Effect of the magnetic field on the thermomechanical flexural wave propagation of embedded sandwich nanobeams

Mustafa Eroğlu, İsmail Esen & Mehmet Akif Koç

Published online: 01 Feb 2024.

Submit your article to this journal ↗

Article views: 177

View related articles ↗

View Crossmark data ↗

Citing articles: 1 View citing articles ↗

Check for updates

Effect of the magnetic field on the thermomechanical flexural wave propagation of embedded sandwich nanobeams

Mustafa Eroğlu[a] (iD), İsmail Esen[b] (iD), and Mehmet Akif Koç[c] (iD)

[a]Engineering Faculty, Mechanical Engineering Department, Sakarya University, Sakarya, Turkey; [b]Engineering Faculty, Mechanical Engineering Department, Karabük University, Karabük, Turkey; [c]Technology Faculty, Mechatronics Engineering Department, Sakarya Applied Sciences University, Sakarya, Turkey

ABSTRACT

This work examines thermo-mechanical bending wave propagation in a sandwich nanobeam using advanced sandwich nanobeam and nanolocal strain gradient elasticity theories. The sandwich nanobeam is a unique structure with biocompatible ceramic ZrO_2 and metal Ti_6Al_4V on the top and bottom sides. Sandwich nanobeam cores have functionally graded materials. This combination gives the nanobeam distinctive qualities and opens up many uses in diverse industries. The wave propagation equation is computed by applying the Navier method to the medium's thermal, Lorentz, and viscoelastic equations of motion. The sandwich nanobeam is analyzed using four distinct models, taking into account its composition of ceramic and metal materials. The various factors that affect sandwich nanobeam bending wave propagation have been extensively studied. In the scenario where the magnetic field intensity is $H_m = 0$, an increase in temperature difference causes the wave frequency of all models (except Model 2) to decrease to zero, resulting in buckling. In Model 2, the sandwich nanobeam exhibits a phase velocity of 0.43 Km/s at $\Delta T = 0$, which subsequently decreases by $\sim$9% to 0.39 km/s at $\Delta T = 500$. These factors include the strength of the magnetic field, the impact of thermal loads, the nonlocal effect, the dimensions of the sandwich nanobeam, and the foundation's influence. The findings of this research will help build nanosensor systems that can work in aerospace applications under extreme temperatures. These findings will contribute to the optimization of the design process, ensuring the reliability and functionality of the nanosensors under severe thermal conditions.

1. Introduction

The dynamic behavior of small-scale systems under different thermal and mechanical loads has garnered significant research interest in recent years. This growing interest can be attributed to the increasing technological demands that require a deeper understanding of how these systems perform under various conditions. On the other hand, functionally graded materials (FGMs) have emerged as a highly sophisticated category of composite materials with the unique characteristic of having varying mechanical properties in one or more directions. This innovative feature sets them apart from traditional materials and opens up many possibilities for their application in various industries. Recently, due to advancements in fabrication methods and the development of

---

miniature systems, there has been a surge of attention toward nanotechnology. This cutting-edge field holds numerous applications in various sectors, including medicine (Morigi et al. 2012; Thrall 2004), engineering (Varadan et al. 2010), food science (Singh et al. 2017), as well as drug delivery and treatments (Emeje et al. 2012; Feizi et al. 2021).

Karami and Ghayesh conducted a study to analyze the vibrational behavior of microshells composed of multilayered materials (Karami and Ghayesh 2023). Studies have been conducted on the relationship between temperature and thermoelastic stresses, static and time-harmonic field solutions, and triaxial magnetic fields in anisotropic structures (Karami, Janghorban, and Tounsi 2017; Vattré and Pan 2022, 2021). Karami et al. used Winkler-Pasternak to study wave propagation in magnetic fields in FG nanoplates with temperature-dependent porosity (Karami, Shahsavari, and Li 2018).

Sandwich structures have become increasingly popular in various industries, including aerospace and automotive machinery, due to their ability to create lightweight yet strong structures. These structures consist of two outer layers, or face sheets, bonded to a lightweight core material. The primary advantage of sandwich structures is their ability to achieve a high strength-to-weight ratio. In the present setting, scholars have undertaken many investigations about sandwich formations. Sayyad et al. analyzed double curvature FGM sandwich shallow shells under static and free vibration conditions (Sayyad, Ghugal, and Kant 2023). Garg et al. conducted a comparative investigation on FG sandwich beams that incorporated varying laws for material property variation (Garg, Chalak, and Chakrabarti 2020). The study by Liu et al. focused on examining the free and forced vibrations of sandwich beams made of FGM. The researchers used the scaled boundary finite element technique to analyze these vibrations (Liu, Hao, et al. 2021). Free vibration of an elastomer sandwich beam, including a magnetorheological (MR) core and a FGM confining layer, was studied by Borogeni et al. in a high-temperature environment (Mirzavand Borojeni et al. 2022). Sahoo et al. focused on examining the effects of geometric nonlinearity on the thermal frequencies and temperature distributions of FG sandwich structures (Sahoo et al. 2022). The vibration performance of a truss sandwich beam with a pyramidal truss core and FGM surface layers at elevated temperatures was examined by Zhang et al. (2022). Yas and Mohammadi conducted an empirical and theoretical investigation into the analysis of free vibrations in a three-layer sandwich beam with functional classification, utilizing the Timoshenko beam theory (Yas and Mohammadi 2020). Youzeraa et al. focused on examining the nonlinear damping and frequency curves of sandwich beams with three layers (Youzera et al. 2023). The study conducted by Burlayenkoa et al. focused on the examination of free vibrations in single-layer and sandwich flat panels made of FGM (Burlayenko, Sadowski, and Altenbach 2022). Shahvari et al. focused on the free vibration response of nano-sized plates resting on elastic foundations against different micromechanical models (Shahsavari and Karami 2022). Also, Shahsavari et al. conducted a study on wave propagation analysis in a viscoelastic system comprising curved nanobeams composed of porous FGMs (Shahsavari, Karami, and Tounsi 2023). Karami et al. examined time-dependent transverse deflection in aragonite nano-sized panels using a quasi-3D curvilinear coordinate model (Karami, Janghorban, and Fahham 2022).

A novel nonlocal strain gradient isogeometric model (NGST) is introduced by (Phung-Van, Ferreira, et al. 2021; Phung-Van and Thai 2022; Thai, Hung, et al. 2023) to analyze functionally graded carbon nanotube-reinforced composite (FG-CNTRC) nanoplates, porous nanoplates, and for magneto-electro-elastic nanoplates (Thai, Fereira, et al. 2023) has used the NGST. Studies by Nguyen et al. (2023) and Phung-Van, Lieu, et al. (2021) present a size-dependent isogeometric analysis of smart functionally graded porous nanoscale plates composed of two piezoelectric materials, utilizing nonlocal elasticity theory (NET), and for multilayer functionally graded graphene platelet-reinforced composite (FG GPLRC) nanoplates. The classical continuum mechanics theory is insufficient in modeling micro-structures' mechanical responses due to its inability to

consider size effects. A modified strain gradient theory (MSGT) is proposed by Hung, Thai, and Phung-Van (2023a).

In a recent study by Vu et al., the dynamic analysis of bidirectional FG sandwich beams was investigated. The study focused on the influence of partial support by a Pasternak foundation on the beams' behavior under a moving mass. This research aimed to gain a better understanding of the structural response of these beams (Vu, Le, and Nguyen 2021). Using a nonlinear finite element approach, Nguyen et al. investigated the impact of various homogenization methods on the significant deformations of bi-phase FGM sandwich beams (Nguyen, Bui, et al. 2022). Xiao and Wang have proposed a novel model for an FGM sandwich nanoplate, including surface effects (Xiao and Wang 2023).

The investigation of buckling has been studied across different models and conditions. For example, the study conducted by Sah and Ghosh focused on examining the phenomena of free vibration and buckling in multi-directional porous FGM sandwich plates (Kumar Sah and Ghosh 2022). Nguyen and Phung's objective is to conduct a thorough examination of the static bending, free vibration, and buckling phenomena exhibited by two-layer FGM plates. These plates are equipped with shear connectors and are supported by elastic foundations (Nguyen and Phung 2023). Le et al. developed a proficient beam element of third-order shear deformation to analyze the free vibration and buckling behavior of bidirectional functionally graded sandwich (BFGSW) beams (Le, Le, and Nguyen 2021). Kim and Cho conducted an investigation of the characteristics of free vibration in FG carbon nanotube-reinforced composites (Kim and Cho 2023). Ghayesh et al. conducted a comprehensive examination of chaos in the viscoelastic nonlinear coupled dynamics of perfectly straight nanotubes subjected to pulsatile fluid flow (Ghayesh, Farajpour, and Farokhi 2020). Belarbi et al. introduced a novel and improved shear deformation beam theory to analyze the bending characteristics of a curved beam made of FG sandwich material (Belarbi, Houari, et al. 2022).

Katili et al. examined the mechanical buckling analysis of sandwich plates made of FGM. To mitigate shear locking, they employed the quadrilateral element Q4γs based on the discrete shear projection method (DSPM) (Katili et al. 2023). Liu et al. proposed a new semi-analytical approach based on the scaled boundary finite element method (SBFEM) to solve the buckling problem of sandwich beams with FGM (Liu, He, et al. 2021). Ellali et al. studied the thermal buckling behavior of FG beams combined with piezoelectric layers (Ellali, Bouazza, and Amara 2022). Utilizing the binary mechanics theory, Gul and Aydogdu researched the buckling analysis of FG nanobeams (Gul and Aydogdu 2021). Lal and Markad conducted a study including the analysis of post-buckling and dynamic nonlinear stability of a sandwich FGM composite beam under in-plane compressive static and periodic loading conditions (Lal and Markad 2021).

Belarbi et al. primarily examined the buckling analysis of curved sandwich beams with functionally graded (FG) properties. The researchers used a three-unknown refined shear theory that was both efficient and straightforward (Belarbi, Garg, et al. 2022). Feri et al. examined the bending behavior of a viscoelastic FGM in three dimensions (Feri, Krommer, and Alibeigloo 2021). Ye et al. have developed a semi-analytical scale boundary finite element model to analyze the buckling behavior of sandwich plates made of FGM (Ye et al. 2022). Madjid and Bouderbab studied the buckling analysis of plates made of FGMs subjected to different load conditions (Hamza Madjid and Bouderba 2022). Bui et al. introduced a methodology for conducting stochastic analysis of vibration and buckling in I-section, FG sandwich thin-walled beams (Bui, Nguyen, and Nguyen 2023). Liu et al. used the scaled boundary finite element technique to study FGM sandwich beam bending (Liu et al. 2023). Civalek et al. investigate the stability analysis of nanobeams with FGM properties, considering size-dependent effects (Civalek, Uzun, and Yaylı 2022).

The impact of porosity on large-scale structures has become a significant study area. Numerous research papers (Derikvand, Farhatnia, and Hodges 2021; Ebrahimi and Jafari 2016; Eltaher et al. 2018; Xu, Karami, and Shahsavari 2021) have delved into porous structures' static

and dynamic behavior. Hung, Thai, and Phung-Van (2023b) present an analysis of the natural vibration of magneto-electro-elastic functionally graded porous (MEE-FGP) plates. These plates are made up of piezoelectric and piezomagnetic materials and have both even and uneven porosity distributions. These investigations have focused on various structures, including conventional, curved, and sandwich beams. Researchers have employed different shear theories to analyze these structures, utilizing analytical and finite element methods. Chaabani et al. introduce a proficient methodology for examining porous FGM plates' buckling and post-buckling characteristics (Chaabani et al. 2023). Chan et al. included an analysis of a sandwich cylindrical panel's critical buckling load and vibration frequencies. The panel consisted of a porous core made of FG material, with surface plates also composed of FG material. The panel was exposed to mechanical stress and heat conditions throughout the analysis (Chan et al. 2022). Chedad et al. examined the impact of porosity on the buckling behavior of FG sandwich plates when subjected to a nonlinear thermal loading (Chedad et al. 2022). Chami et al. conducted a study that employed the theory of an enhanced shear deformable beam to investigate the impact of pores on the natural frequencies of an FG sandwich beam with simply supported ends (Chami, Kahil, and Hadji 2022). Karakoti et al. proposed a finite element formulation for the purpose of analyzing and comparing the nonlinear transient behavior of sandwich plates and shell panels made of porous FGM (Karakoti, Pandey, and Kar 2022). Nguyen et al. provide a methodology to address the issue of free vibration in rotating FG porous sandwich cylindrical shells (Nguyen, Tran, et al. 2022).

Predicting the propagation of waves in micro/nano materials is a crucial aspect when it comes to designing with precision. Extensive research has been conducted on the topic of wave propagation. The study conducted by Li et al. explores the behavior of wave propagation in porous FG piezoelectric nanoplates, with a focus on the influence of size on this phenomenon (Li et al. 2023). Karami et al. propose a novel method for analyzing wave dispersion in anisotropic double-curved nanoshells (Karami, Janghorban, and Tounsi 2018). In a recent study conducted by Faroughi et al., the researchers investigated the wave propagation in a rotating 2D FGM porous nanobeam. Al-Furjan et al. investigated using porous FGMs and magnetostrictive nanocomposite layers to improve the stiffness and control of wave propagation in micro-aircraft wings (Al-Furjan et al. 2023). Karami et al. study size-dependent guided wave propagation in porous, functionally graded nanoplates (Karami, Janghorban, and Li 2018). Furjan et al. studied the wave propagation characteristics of micro-sandwich beams. The sandwich beam in issue comprises three distinct layers: the core layer made of auxetic honeycomb material, the top layer made of piezoelectric material, and the bottom layer made of 2D-FGM (Al-Furjan et al. 2022). Karami et al. aim to study the distribution of elastic waves in double-curved nanoshells (Karami, Janghorban, and Tounsi 2020). Karami et al. investigated the elastic bulk wave properties of a functionally graded (FG) anisotropic nanoshell with double curvature (Karami, Janghorban, and Tounsi 2019). The objective of the study conducted by Avcar et al. is to examine the natural frequencies of sandwich beams with different configurations, specifically focusing on sigmoid FG, by employing high-order shear deformation theory (Avcar, Hadji, and Civalek 2021). Hassainea et al. examined the impact of transverse fractures on the natural frequencies of Euler-Bernoulli FG beams (Hassaine et al. 2022). Ebrahimi and Sepahvand aimed to examine the impact of the auxiliary layer on wave propagation and the resulting effective characteristics in cylindrical sandwich shells (Ebrahimi and Sepahvand 2023). Al-Osta investigated the wave propagation characteristics of a plate composed of FG materials adopting the exponential law, with additional support from viscoelastic foundations (Al-Osta 2023). Eyvazian et al. examined the characteristics of damped propagation in bulk-type waves within a sandwich nanoplate (Eyvazian et al. 2022).

1.1. Novelty of the study

The literature lacks studies on wave propagation in FGM sandwich nanobeams. This study examines the thermomechanical wave propagation behavior of sandwich-embedded nanobeams under

the influence of a magnetic field. The investigation focuses on the potential applications of this behavior in advanced bioapplications, such as micro and nano-sized biorobotic systems and sensors. This study demonstrates a significant and practical approach to altering the thermomechanical wave propagation behavior of the magnetic field nanobiosensor beam. Furthermore, the viscoelastic environment's influence on the nanobeam's wave behavior is discussed, as bioapplication environments typically exhibit viscoelastic properties.

2. Sandwich embedded nanobeam

The nanobeam sandwich being investigated consists of three layers and is seen in Fig. 1. It is characterized by its dimensions L and b. The x and y axes are situated inside the median plane at $z = 0$. Furthermore, the origin is positioned at the corner of the beam. The sandwich nanobeam's exterior sides are positioned at $z = (\pm h/2)$. The vertical locations of the bottom surface, the two interfaces between the core layers, and the top surface are denoted as $h_0 = -h/2$, h_1, h_2, and $h_3 = +h/2$, respectively.

The sandwich nanobeam's core consists of an FGM with properties that gradually change along the thickness in the z direction. It should be noted that the FGM layers consist of a composite of metal and ceramic, whereas the surfaces are comprised of ceramic, metal, or a hybrid combination of these materials. The volume fraction of the constituent materials is a determining factor for the properties of FGM nanobeams. Furthermore, it is assumed that the Poisson's ratio remains constant. Whereas, the effective material properties, including the elastic modulus E and the coefficient of thermal expansion α, are not assumed to be constant for each layer.

The formation dispersion of the nanobeam might vary depending on the specific manufacturing processes used. Empirical investigations have shown that the assumption that beams consist only of a single material inadequately captures the decline in stiffness exhibited by beams. Consequently, this research anticipates the presence of five distinct distribution functions to represent the material distribution. As shown in Fig. 2, the beam exhibits several compositions, including an entire ceramic composition, a complete metal composition, a core composed of metal with ceramic surfaces, a core composed of ceramic with metal surfaces, and a core composed of FGM with ceramic-metal mixture surfaces. The core component of the Model 5 is made of FGM, while the surfaces are made up of a complex combination of ceramics and metal. In this particular investigation, the upper and lower surfaces are made up of a blend of ceramics and metals that is around fifty percent each.

The temperature's impact is crucial for accurately predicting the behavior of a structure. The effective Poisson's ratio ν_{ef}, modulus of elasticity E_{ef}, the coefficients of thermal expansion κ_{ef}, and conductivity ψ_{ef} are considered temperature-dependent properties and can be defined using a nonlinear function of temperature (Touloukian 1966, 1967).
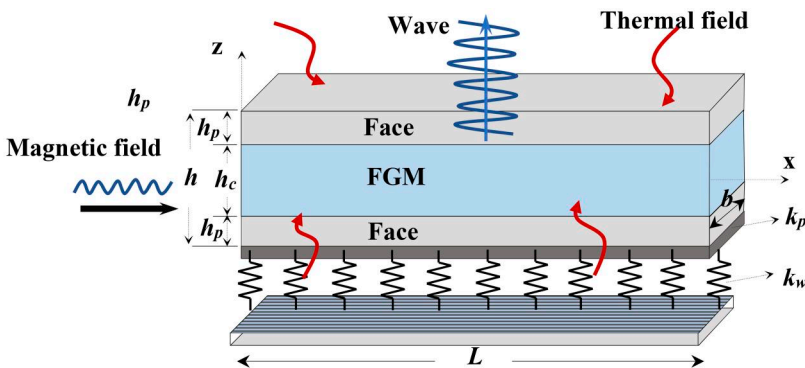

Figure 1. Configuration of a sandwich embedded nanobeam in thermal and magnetic fields.
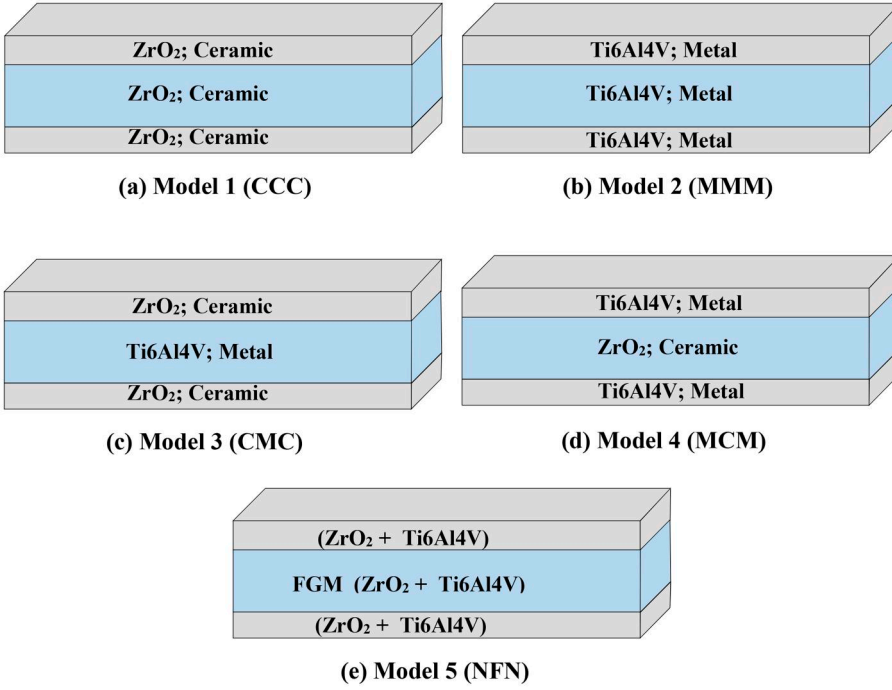
Figure 2. Four models of porosity distribution across the thickness (a) Model 1; Ceramic-Ceramic-Ceramic (CCC), (b) Model 2; Metal-Metal-Metal (MMM), (c) Model 3; Ceramic-Metal-Ceramic (CMC), (d) Model 4; Metal-Ceramic-Metal, and (e) Model 5; Zr + Ti-FGM-Zr + Ti (NFN).

$$P = P_0\left(P_{-1}T^{-1} + 1 + P_1 T + P_2 T^2 + P_3 T^3\right) \tag{1}$$

The temperature-dependent properties of a constituent, represented by P, are characterized by the material's P_0, P_{-1}, P_1, P_2, and P_3 values, corresponding to the orders (-1, 0, 1, 2, and 3) of temperature T (in Kelvin). Furthermore, the mass density $\rho(z)$ is primarily determined by the effective material properties and is only influenced to a small extent by changes in temperature.

2.1. Temperature rises

This section provides the equations for uniform temperature increase (UTR), linear temperature increase (LTR), and nonlinear temperature increase (NLTR) along the thickness of the nanobeam. The equation used to uniformly raise the temperature of a FGM nanobeam with an initial temperature $T_0 = 300\,\mathrm{K}$ to its final temperature T in a stress-free state with uniform temperature rise (UTR) is as follows:

$$\Delta T = T - T_0 \tag{2}$$

The temperature distribution within a beam extending along the z-direction can be determined using the following equation, assuming a linear temperature rise (LTR) from the bottom surface (T_b) to the top surface (T_t) along the thickness (Kiani and Eslami 2013):

$$T(z) = T_b + (T_t - T_b)\left(\frac{h + 2z}{2h}\right) \tag{3}$$

The given one-dimensional heat transfer equation in a steady-state scenario can be solved using known temperature boundary conditions to determine the temperatures of the nanobeam's top surface (T_t) and bottom surface (T_b). This analysis is applicable when nonlinear temperature

raises (NLTR) occur throughout the nanobeam's thickness (Zhang 2014).

$$-\frac{d}{dz}\left(\kappa(z)\frac{dT}{dz}\right) = 0, T\left(\frac{h}{2}\right) = T_t, \quad T\left(-\frac{h}{2}\right) = T_b \tag{4}$$

Hence, given a set of specified boundary conditions, the temperature at any point z, which extends throughout the thickness, can be determined.

$$T(z) = T_b + \frac{(T_t - T_b)}{\int_{-\frac{h}{2}}^{\frac{h}{2}} \frac{1}{\psi(z)} d(z)} \int_{-\frac{h}{2}}^{z} \psi(z) dz \tag{5}$$

3. Non-local strain gradient theory

In accordance with the nonlocal strain gradient theory (NSGT), the normal and shear stress at any given point can be mathematically represented as stated in reference (Lim, Zhang, and Reddy 2015):

$$\begin{aligned} \sigma_{xx}^t &= \sigma_{xx}^c - \nabla^2 \sigma_{xx}^h \\ \sigma_{xz}^t &= \sigma_{xz}^c - \nabla^2 \sigma_{xz}^h. \end{aligned} \tag{6}$$

In which:

$$\begin{aligned} \sigma_{xx}^c &= \int_V E(z)\alpha_0(\boldsymbol{x}', \boldsymbol{x}, e_0 a)\varepsilon_{xx}'(\boldsymbol{x}')dV', \\ \sigma_{xx}^h &= l_m^2 \int_V E(z)\alpha_1(\boldsymbol{x}', \boldsymbol{x}, e_1 a)\nabla\varepsilon_{xx}'(\boldsymbol{x}')dV', \\ \sigma_{xz}^c &= \int_V G(z)\alpha_0(\boldsymbol{x}', \boldsymbol{x}, e_0 a)\gamma_{xz}'(\boldsymbol{x}')dV', \\ \sigma_{xz}^h &= l_m^2 \int_V G(z)\alpha_1(\boldsymbol{x}', \boldsymbol{x}, e_1 a)\nabla\gamma_{xz}'(\boldsymbol{x}')dV'. \end{aligned} \tag{7}$$

In this context, $\sigma^{"c"}$ and, $\sigma^{"h"}$ denote the classical and higher-order normal and shear stresses, respectively, while ∇ signifies the Laplacian operator. The nanoscale size effect is characterized by the material parameter l_m. The nonlocality coefficients are denoted as $e_0 a$ and $e_1 a$ (Eringen 1983), accompanied by the classical and higher-order nonlocal kernel functions α_0 and α_1. Assuming the equality of $e_0 a$ and $e_1 a$, and employing a linear differential operator, one can derive the subsequent equation in relation to the nonlocal strain gradient theory (NSGT) (Lim, Zhang, and Reddy 2015):

$$\begin{aligned} \left[1 - (e_0 a)^2 \nabla^2\right]\sigma_{xx}^t &= \left[1 - l_m^2 \nabla^2\right]E(z)\varepsilon_{xx} \\ \left[1 - (e_0 a)^2 \nabla^2\right]\sigma_{xz}^t &= \left[1 - l_m^2 \nabla^2\right]G(z)\gamma_{xz} \end{aligned} \tag{8}$$

where $\sigma^{"t"}$ represents the total stress and ε_{xx} and γ_{xz} denote the normal and shear strains, Equation (8) can be expressed as follows:

$$\begin{aligned} \sigma_{xx}^t - (e_0 a)^2 \frac{\partial^2 \sigma_{xx}^t}{\partial x^2} &= \left[\varepsilon_{xx} - l_m^2 \frac{\partial^2 \varepsilon_{xx}}{\partial x^2}\right]E(z) \\ \sigma_{xz}^t - (e_0 a)^2 \frac{\partial^2 \sigma_{xz}^t}{\partial x^2} &= \left[\gamma_{xz} - l_m^2 \frac{\partial^2 \gamma_{xz}}{\partial x^2}\right]G(z) \end{aligned} \tag{9}$$

For nonlocal elasticity and gradient elasticity, a recent study (Askes and Aifantis 2009) has utilized higher-order elasticity theories to forecast the dispersion properties of flexural waves in carbon nanotubes (CNTs).

4. Mathematical formulation

To account for the shear deformation effect, we employ a sophisticated sinusoidal higher-order shear deformation theory (Tounsi et al. 2013), which incorporates the following displacement field within the beam.

$$u_1(x, z, t) = u(x, t) - z\frac{\partial w}{\partial x} + f(z)\phi(x, t)$$
$$u_2(x, z, t) = 0$$
$$u_3(x, z, t) = w(x, t)$$

(10)

Let u_1, u_2, and u_3 denote the displacements in the x, y, and z directions, respectively. Additionally, let $\phi(x, t)$ represent the rotation of the cross-section, while $w(x, t)$ and $u(x, t)$ represent the transverse and axial displacements in the neutral plane. Based on the trigonometric shape function $f(z) = z - \frac{h}{\pi}\sin\left(\frac{\pi}{h}z\right)$ and the displacement field, the strains can be mathematically represented as (Li and Hu 2016; Ma, Gao, and Reddy 2008).

$$\varepsilon_{xx} = \varepsilon_{xx}^0 - z\varepsilon_{xx}^1 + f(z)\varepsilon_{xx}^2, \gamma_{xz} = \frac{df(z)}{dz}$$

(11)

In which

$$\varepsilon_{xx}^0 = \frac{\partial u}{\partial x} - \frac{1}{2}\left(\frac{\partial w}{\partial x}\right)^2, \varepsilon_{xx}^1 = \frac{\partial^2 w}{\partial x^2}, \varepsilon_{xx}^2 = \frac{\partial \phi_x}{\partial x}$$

(12)

4.1. Classical stress-strain relations

The constitutive equation pertaining to the strains (17) is as follows:

$$\begin{Bmatrix} \sigma_{xx} \\ \tau_{xz} \end{Bmatrix} = \begin{bmatrix} Q_{11} & 0 \\ 0 & Q_{66} \end{bmatrix} \begin{Bmatrix} \varepsilon_{xx} \\ \gamma_{xz} \end{Bmatrix}$$

(13)

Given the provided values of stiffness:

$$Q_{11} = \frac{E(z)}{1 - v^2}, Q_{66} = \frac{E(z)}{2(1 + v)}$$

(14)

By utilizing linear elasticity principles, the end force and moment resultants of an infinitesimally small beam element can be characterized as follows:

$$\begin{Bmatrix} N_{xx} \\ M_{xx} \\ P_{xx} \end{Bmatrix} = \int_{-\frac{h}{2}-hp}^{-h/2} \begin{Bmatrix} 1 \\ z \\ f(z) \end{Bmatrix} \sigma_{xx}dz + \int_{-h/2}^{h/2} \begin{Bmatrix} 1 \\ z \\ f(z) \end{Bmatrix} \sigma_{xx}dz + \int_{h/2}^{\frac{h}{2}+hp} \begin{Bmatrix} 1 \\ z \\ f(z) \end{Bmatrix} \sigma_{xx}dz$$
$$Q_{xz} = \int_{-\frac{h}{2}+hp}^{-h/2} \frac{df(z)}{dz}\tau_{xz}dz + \int_{-h/2}^{h/2} \frac{df(z)}{dz}\tau_{xz}dz + \int_{h/2}^{\frac{h}{2}+hp} \frac{df(z)}{dz}\tau_{xz}dz$$

(15)

By substituting the strains from Equations (13) and (14) into Equation (15), the force resultants can be derived.

$$\begin{Bmatrix} N_{xx} \\ M_{xx} \\ P_{xx} \end{Bmatrix} = \begin{bmatrix} A_{11} & B_{11} & C_{11} \\ B_{11} & D_{11} & F_{11} \\ C_{11} & F_{11} & H_{11} \end{bmatrix} \begin{Bmatrix} \varepsilon_{xx}^0 \\ \varepsilon_{xx}^1 \\ \varepsilon_{xx}^2 \end{Bmatrix},$$
$$Q_{xz} = J_{66}\gamma_{xz}.$$

(16)

with the following stiffness coefficients:

$$(A_{11}, B_{11}, C_{11}, D_{11}, F_{11}, H_{11})$$

$$= b \int_{-\frac{h}{2}-hp}^{-\frac{h}{2}} \left[1, z, z^2, f(z), zf(z), f(z)^2\right] Q_{11} dz + b$$

$$\int_{-h/2}^{h/2} \left[1, z, z^2, f(z), zf(z), f(z)^2\right] Q_{11} dz + b \tag{17}$$

$$\int_{h/2}^{\frac{h}{2}+hp} \left[1, z, z^2, f(z), zf(z), f(z)^2\right] Q_{11} dz J_{66}$$

$$= b \int_{-\frac{h}{2}-hp}^{-h/2} \left(\frac{df(z)}{dz}\right)^2 Q_{66} dz + b \int_{-h/2}^{h/2} \left(\frac{df(z)}{dz}\right)^2 Q_{66} dz + b \int_{h/2}^{\frac{h}{2}+hp} \left(\frac{df(z)}{dz}\right)^2 Q_{66} dz.$$

4.2. Magnetic field and thermal force

In this study, the evaluation of the magnetic field's effect is conducted using Maxwell's equations (Arani and Jalaei 2017; Kraus 1992), which describe the magnetic field intensity (**H**), current density vector (**J**), magnetic field vector (**h**), electric field vector (**e**), and magnetic field permeability (ε).

$$J = \nabla \times h, \nabla \times e = -\varepsilon \frac{\partial \mathbf{h}}{\partial t}, \nabla . \mathbf{h} = 0 \tag{18}$$

$$e = -\varepsilon \left(\frac{\partial U}{\partial t} \times H\right), \mathbf{h} = \nabla \times (U \times H) \tag{19}$$

In this context, let $\boldsymbol{U} = u\vec{i} + v\vec{j} + w\vec{k}$ represent the displacement vector. Given a nanobeam subjected to a horizontal magnetic field with an intensity of $\mathbf{H} = H_x\vec{i}$, the magnetic field vector can be expressed as:

$$\mathbf{h} = -\bar{H}_x \left(\frac{\partial v}{\partial y} + \frac{\partial w}{\partial z}\right)\vec{i} + \bar{H}_x \frac{\partial v}{\partial x}\vec{j} + \bar{H}_x \frac{\partial w}{\partial x}\vec{k} \tag{20}$$

The Lorentz force resulting from the interaction between a magnetic field and a charged particle can be derived using the following equation:

$$f_m = f_{mx}\vec{i} + f_{my}\vec{j} + f_{mz}\vec{k} = \varepsilon(\mathbf{J} \times \mathbf{H})$$

$$= \eta \left[0\vec{i} + \bar{H}_x^2 \left(\frac{\partial^2 v}{\partial x^2} + \frac{\partial^2 v}{\partial y^2} + \frac{\partial^2 w}{\partial y \partial z}\right)\vec{j} + \bar{H}_x^2 \left(\frac{\partial^2 w}{\partial x^2} + \frac{\partial^2 w}{\partial z^2} + \frac{\partial^2 v}{\partial y \partial z}\right)\vec{k}\right] \tag{21}$$

In the transverse z direction, the Lorentz force can be expressed concisely as:

$$f_{mz} = \varepsilon \bar{H}_x^2 \left(\frac{\partial^2 w}{\partial x^2} + \frac{\partial^2 w}{\partial z^2} + \frac{\partial^2 v}{\partial y \partial z}\right) \tag{22}$$

Ultimately, the Lorentz force can be defined as per equations (21) and (22).

$$F_l = \int_{-h/2}^{h/2} f_{mz} dz = \varepsilon h \bar{H}_x^2 \frac{\partial^2 u_3}{\partial x^2} = \varepsilon h \bar{H}_x^2 \frac{\partial^2 w}{\partial x^2} \tag{23}$$

As a consequence of the consistent rise in temperature, the quantities of force N^T and moment M^T can be precisely characterized.

$$N^T = b \int_{-h/2}^{h/2} E(z, T)\psi(z, T)\Delta T dz \tag{24}$$

$$M^T = b \int_{-h/2}^{h/2} E(z, T)z\psi(z, T)\Delta T dz \tag{25}$$

4.3. Variational statements

The application of Hamilton's principle (Reddy 2007) is employed in this study to derive the equations of motion for the sandwich nanobeam under consideration.

$$\int_{t1}^{t2} (\delta T - \delta U + \delta V) dt = 0. \tag{26}$$

U, T, and V represent the respective energies associated with strain, kinetic, and external potential. Given the various stresses, force resultants, and strains, the total deformation energy U of the embedded sandwich beam can be mathematically represented as follows:

$$U = \frac{1}{2} \int_V (\sigma_{xx}\varepsilon_{xx} + \tau_{xz}\gamma_{xz}) dV,$$
$$U = \frac{1}{2} \int_0^L \left(N_{xx}\varepsilon_{xx}^0 + M_{xx}\varepsilon_{xx}^1 + P_{xx}\varepsilon_{xx}^2 + Q_{xz}\gamma_{xz}\right) dx \tag{27}$$

For the assumed displacements, the kinetic energy is written as:

$$T = \frac{1}{2} \int_0^l \int_A \rho(z) \left[\left(\dot{u}^2 + \dot{w}^2\right)\right] dA dx \tag{28}$$

The external potential energy is expressed as a function of the thermal load N^T, magnetic field intensity $\bar{H}_x$, spring k_w, shear k_p foundations, and the transverse load $q(x, t)$.

$$\delta V = \int_\Omega \left[k_w w(x, t)\delta w + k_p \frac{\partial^2 w}{\partial x^2} w(x, t)\delta w + q(x, t)\delta w - N^T \frac{\partial^2 w}{\partial x^2} w(x, t)\delta w + \varepsilon h \bar{H}_x^2 \frac{\partial^2 w}{\partial x^2} w(x, t)\delta w\right] d\Omega \tag{29}$$

By substituting Equations (27)–(29) into Hamilton's principle (27) and performing integration by parts, the displacement equations for the current sinusoidal shear deformation theory can be obtained by setting the coefficients of $\delta u, \delta w$, and $\delta\phi_x$ to zero.

$$\delta u: \frac{\partial N_{xx}}{\partial x} = I_0 \frac{\partial^2 u}{\partial t^2} - I_1 \frac{\partial^3 w}{\partial x \partial t^2} + I_3 \frac{\partial^2 \phi_x}{\partial t^2},$$

$$\delta w: \frac{\partial^2 M_{xx}}{\partial x^2} = q(x, t) + I_0 \frac{\partial^2 w}{\partial t^2} + I_1 \frac{\partial^3 u}{\partial x \partial t^2} - I_2 \frac{\partial^4 w}{\partial x^2 \partial t^2} + I_4 \frac{\partial^3 \phi_x}{\partial x \partial t^2}, \tag{30}$$

$$\delta \phi_x: \frac{\partial P_{xx}}{\partial x} - Q_{xz} = I_3 \frac{\partial^2 u}{\partial t^2} - I_4 \frac{\partial^3 w}{\partial x \partial t^2} + I_5 \frac{\partial^2 \phi_x}{\partial t^2}$$

The inertia coefficients are as follows:

$$(I_0, I_1, I_2, I_3, I_4, I_5) = b \int_{-\frac{h}{2}-hp}^{-\frac{h}{2}} \rho(z)\left(1, z, z^2, f(z), zf(z), f(z)^2\right) dz$$

$$+ b \int_{-h/2}^{h/2} \rho(z)\left(1, z, z^2, f(z), zf(z), f(z)^2\right) dz$$

$$+ b \int_{h/2}^{\frac{h}{2}+hp} \rho(z)\left(1, z, z^2, f(z), zf(z), f(z)^2\right) dz \quad (31)$$

By incorporating the nonlocal strain gradient elasticity into Equation (10) and utilizing the force-displacement relations expressed in Equation (16), we can establish the governing equations of motion for the higher-order FG porous nanobeam.

$$\left(1 - l_m^2 \frac{\partial^2}{\partial x^2}\right)\left(A_{11}\frac{\partial^2 u}{\partial x^2} - B_{11}\frac{\partial^3 w}{\partial x^3} + C_{11}\frac{\partial^2 \phi}{\partial x^2}\right) + \left(1 - (e_0 a)^2 \frac{\partial^2}{\partial x^2}\right)\left(-I_0\frac{\partial^2 u}{\partial t^2} + I_1\frac{\partial^3 w}{\partial x \partial t^2} - I_3\frac{\partial^2 \phi_x}{\partial t^2}\right) = 0,$$

$$\left(1 - l_m^2 \frac{\partial^2}{\partial x^2}\right)\left(B_{11}\frac{\partial^3 u}{\partial x^3} - D_{11}\frac{\partial^4 w}{\partial x^4} + F_{11}\frac{\partial^3 \phi}{\partial x^3}\right) + \left(1 - (e_0 a)^2 \frac{\partial^2}{\partial x^2}\right)\left(\left(\varepsilon h \bar{H}_x^2 - N^T + k_p\right)\right)$$

$$\frac{\partial^2 w}{\partial x^2} + k_w - q(x,t) - I_0\frac{\partial^2 w_0}{\partial t^2} - I_1\frac{\partial^3 u}{\partial x \partial t^2} + I_2\frac{\partial^4 w}{\partial x^2 \partial t^2} - I_4\frac{\partial^3 \phi_x}{\partial x \partial t^2}\right) = 0,$$

$$\left(1 - l_m^2 \frac{\partial^2}{\partial x^2}\right)\left(C_{11}\frac{\partial^2 u}{\partial x^2} - F_{11}\frac{\partial^3 w}{\partial x^3} + H_{11}\frac{\partial^2 \phi}{\partial x^2} + J_{66}\phi\right) + \left(1 - (e_0 a)^2 \frac{\partial^2}{\partial x^2}\right)\left(-I_3\frac{\partial^2 u}{\partial t^2} + I_4\frac{\partial^3 w}{\partial x \partial t^2} - I_5\frac{\partial^2 \phi_x}{\partial t^2}\right) = 0. \quad (32)$$

4.4. Analytical solution

Given the assumption of a periodic solution in time, the displacements $u(x,t)$, $w(x,t)$, and $\phi(x,t)$ in Equation (10) can be approximated using Navier's approach for the simply supported boundary conditions, as outlined in the following manner (Ebrahimi et al. 2022):

$$u(x,t) = U_n e^{i(\beta x - \omega_n t)},$$
$$w(x,t) = W_n e^{i(\beta x - \omega_n t)},$$
$$\phi(x,t) = W_s e^{i(\beta x - \omega_n t)}, \quad (33)$$
$$\beta = \left(\frac{n\pi}{L}\right).$$

The solution of Equation (33) satisfies the classical and non-classical boundary conditions at $x = 0$ and $x = L$, which describe the unknowns U_n, W_n and Φ_n.

The classical:

$$N_{xx} = 0, w = 0, M = 0. \quad (34)$$

And the non-classical:

$$\frac{\partial u}{\partial x} = 0, Q_{xz}^h = 0, \frac{\partial \phi}{\partial x} = 0 \quad (35)$$

In Equation (33), the variable i represents the imaginary unit, which is equal to the square root of the negative one. The variable ω_n denotes the nth natural vibration frequencies. By substituting Equation (33) into Equation (34), we obtain the subsequent equation for the eigenvalues:

$$\left(\mathbf{K} - \omega_n^2\mathbf{M}\right)\mathbf{d} = 0 \tag{36}$$

In this context, let $\mathbf{d} = \left\{ U_n \ W_n \ \Phi_n \right\}^T$ denote the vector of defined unknowns. M and K matrices correspond to the mass and stiffness matrices, respectively. The coefficients for these matrices can be found in Appendix A.

By equating the determinant of the matrix $(\mathbf{K} - \omega_{mn}^2\mathbf{M})$ to zero and solving for the frequency ω_{mn}, the angular frequencies of the waves corresponding to the modes M_n can be determined.

$$\omega_n = M_n(k_n) \tag{37}$$

After establishing the angular frequencies using Equation (37), the phase velocity of each mode can be derived.

$$v_n = \frac{\omega_n}{k_n}, n = 1, 2, 3 \tag{38}$$

In the limit, as the wave number k approaches infinity, the escape frequency of the nanoplate is determined.

$$\tilde{\omega}_n = \lim_{k \to \infty} \frac{\omega_n}{2\pi}, n = 1, 2, 3, \ldots \tag{39}$$

In parametric studies, the utilization of the following dimensionless parameters is customary:

$$H_m = \frac{\varepsilon h \bar{H}_x^2 L^2}{D_c}, D_C = \frac{Q_{11c}h^3}{12(1 - v_c^2)} \tag{40}$$

In which H_m represents the magnetic field intensity parameter. The elasticity modulus and Poisson's ratio of ceramic material (ZrO$_2$) at room temperature are denoted as Q_{11c} and v_c, respectively.

5. Numerical analyses and verification

To validate the current methodology, a comparative study is performed, utilizing the analytical and finite element methods as described in the existing literature. The study focuses on a simply supported FM beam comprising Alumina (99.5%) and Aluminum. Table 2 presents a comparison of the dimensionless fundamental frequency λ_1, calculated using Equation (41) for the same conditions as the material properties (Esen 2019; Nguyen, Gan, and Le 2013; Sina, Navazi, and Haddadpour 2009) provided in Table 1. Table 2 demonstrates a strong concurrence between the results obtained from the present approach and those derived from the finite element method (Nguyen, Gan, and Le 2013) and the analytical method (Sina, Navazi, and Haddadpour 2009).

$$\lambda_1 = \omega_1 L^2 \left(\int_{-h/2}^{h/2} \rho(z)dz \right)^{0.5} \left(h^2 \int_{-h/2}^{h/2} E(z)dz \right)^{-0.5} \tag{41}$$

When subjected to dynamic loads, another comparative analysis is performed on the forced vibration behavior of an FGM beam consisting of Alumina and SUS304. The material properties used in this study are based on the data provided in Table 3, which is sourced from reference (Khalili,

Table 1. The material properties of the constituents in functionally graded materials (FGMs) at standard room temperature (Nguyen, Gan, and Le 2013; Sina, Navazi, and Haddadpour 2009).

Properties	Aluminum (metal)	Alumina (Al$_2$O$_3$) (ceramic)
ρ (kg/m^3)	2700	3800
E (GPa)	70	380
υ	0.23	0.23

Table 2. The dimensionless frequency (λ_1) comparisons of the simply supported (SS) functionally graded material (FGM) beam composed of Al_2O_3 and Aluminum.

Power-law exponent p		Fundamental frequency, λ_1		
	Refs.	$L/h = 10$	$L/h = 30$	$L/h = 100$
0	Present	2.7971	2.8431	2.8480
	From Nguyen, Gan, and Le (2013)	2.7970	2.8430	2.8480
	From Sina, Navazi, and Haddadpour (2009)	2.8026	2.8438	2.8486
	From Esen (2019)	2.8027	2.8458	2.8488
0.3	Present	2.6951	2.7371	2.7421
	From Nguyen, Gan, and Le (2013)	2.6950	2.7370	2.7420
	From Sina, Navazi, and Haddadpour (2009)	2.6992	2.7368	2.7412
	From Esen (2019)	2.6953	2.7361	2.7421

Table 3. The coefficients of temperature dependent properties.

Material	Property	P_{-1}	P_0	P_1	P_2	P_3
ZrO_2	ρ (kg/m^3)	0	5680	0	0	0
	E (Pa)	0	244.27×10^9	-1.371×10^{-3}	1.214×10^{-6}	-3.681×10^{-10}
	υ	0	0.2882	1.133×10^{-4}	0	0
	α (1 K^{-1})	0	12.766×10^{-6}	-1.491×10^{-3}	1.006×10^{-5}	-6.778×10^{-11}
	ψ (W/mK)	0	1.7	1.276×10^{-4}	6.648×10^{-8}	0
Ti_6Al_4V	ρ (kg/m^3)	0	4512	0	0	0
	E (Pa)	0	122.56×10^9	-4.586×10^{-4}	0	0
	υ	0	0.2884	1.121×10^{-4}	0	0
	α (1 K^{-1})	0	7.5788×10^{-6}	6.638×10^{-4}	-3.147×10^{-6}	0
	ψ (W/mK)	0	15.397	-1.264×10^{-3}	2.092×10^{-6}	-7.223×10^{-10}

Table 4. For a FGM nanobeam with $L = 100$ nm, $h = 0.1$ nm, compare the dimensionless frequency λ_i for a range of material grading indices and nonlocal factors.

$\frac{(e_0 a)^2}{nm^2}$	p = 0			p = 0.2			p = 5		
	Present	Rahmani and Pedram (2014)	Ebrahimi and Salari (2015b)	Present	Rahmani and Pedram (2014)	Ebrahimi and Salari (2015b)	Present	Rahmani and Pedram (2014)	Ebrahimi and Salari (2015b)
0	9.86312	9.8631	9.86315	8.68951	8.6895	8.68954	5.93892	5.9389	5.93894
1	9.40972	9.4097	9.40973	8.29008	8.2901	8.29007	5.66591	5.6659	5.66592
2	9.01355	9.0136	9.01358	7.94107	7.9411	7.94106	5.42742	5.4274	5.42739
3	8.66361	8.6636	8.66360	7.63271	7.6327	7.63272	5.21663	5.2166	5.21665
4	8.35144	8.3515	8.35146	7.35770	7.3577	7.35772	5.02873	5.0287	5.02869

Jafari, and Eftekhari 2010). The results obtained in this study are then compared with the findings reported in references (Khalili, Jafari, and Eftekhari 2010) and (Şimşek and Kocatürk 2009). Table 4 presents the comparisons of normalized maximum midpoint responses, revealing a close correspondence between the outcomes obtained from the current methodology and those documented in existing scholarly literature.

The dimensionless frequencies $\lambda_i = \omega_i L^2 \sqrt{\rho_c A/E_c I}$, which account for the nonlocality effect, are calculated using the current procedure. These frequencies are obtained by multiplying the angular frequencies ω_i by the square of the length scale L, and then dividing by the square root of the product of the density ρ_c, the speed of sound in the material A, the Young's modulus E_c, and the moment of inertia I. The resulting values are then compared with the frequencies reported in Table 3 of the literature for an FGM nanobeam with the same material properties as mentioned earlier. The nanobeam has a length L of 100 nm, a height h equal to one-tenth of L, and a width b equal to h. Table 4 presents the results of the comparison, indicating a strong concurrence between the outcomes of the current methodology for the nonlocality effect and the findings reported by previous studies (Ebrahimi and Salari 2015a; Rahmani and Pedram 2014).
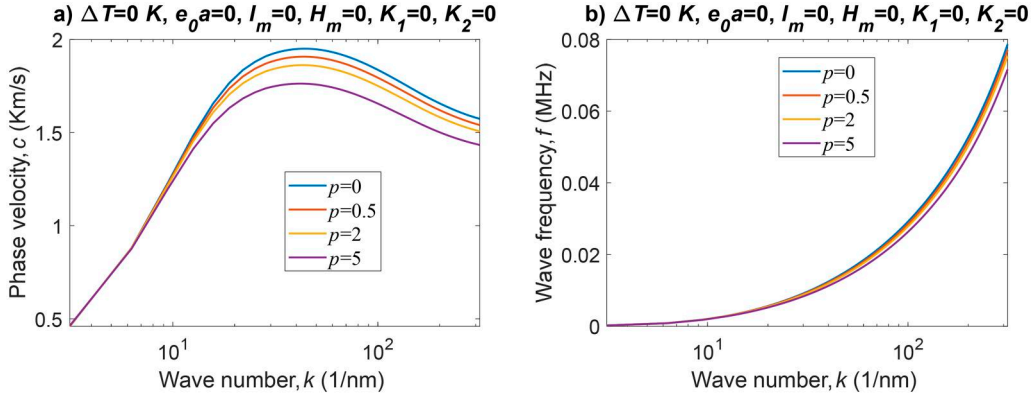
Figure 3. Variation of the phase velocity and wave frequency of the sandwich nanobeam *vs.* wave number k (1/nm) depending on the power law index of the core beam for $p = 0, 0.5, 2, 5$; (a) Phase velocity (km/s); (b) Wave frequency (MHz); $L = 100$ nm, $h = L/10$, $b = h$, $h_c = 0.6h$, $h_p = 0.2h$; Material ratios of faces Ti = 0.5, Zr = 0.5; Ti: Ti_6Al_4V, Zr:ZrO_2; the other parameters: temperature rise $\Delta T = 0$ K, nonlocal parameter $e_0a = 0$, material size parameter $l_m = 0$, magnetic field intensity $H_m = 0$, spring foundation parameter $K_1 = 0$, and shear foundation parameter $K_2 = 0$.

In Fig. 3, the variation of the sandwich nanobeam wave frequency (Fig. 3b) and phase velocity (Fig. 3a) according to the wave number for four different power law index $p = 0, 0.5, 2, 5$ showing the material component of the FG core of the sandwich nanobeam is given. Here, the core beam consists of the functional grading of the biocompatible materials metal (Ti_6Al_4V) and ceramic (zirconia; ZrO_2) material components, while the faces of the sandwich nanobeam are assumed to consist of a homogeneous mixture of these two materials at Ti = 0.5 and Zr = 0.5 volumetric ratios. The length of the nanobeam was taken as $L = 100$ nm, thickness $h = L/10$, core thickness $h_c = 0.6h$, surface sandwich sections of equal height, and $h_p = 0.2h$. At $p = 0$, the core part consists entirely of zirconium. Since the material of the surfaces is half zirconia, 80% of the nano sandwich beam material consists of zirconia, and 20% is Ti_6Al_4V. This ratio is calculated from core h_c, surface hp thicknesses, and power law index. Accordingly, the total ceramic ratio is calculated as $C = 0.6h(1) + 0.2(0.5)h_p(2)$. Here, 0.6 indicates the core part height ratio, (1) the core part consists entirely of ceramic because the power law index is zero, 0.2 indicates the surface thickness ratio, 0.5 indicates 50% of the zirconia ratio in the surface, and (2) the surface has two parts. The other parameters are temperature rise $\Delta T = 0$ K, nonlocal parameter $e_0a = 0$, material size parameter $l_m = 0$, magnetic field intensity $H_m = 0$, spring foundation parameter $K_1 = 0$, and shear foundation parameter $K_2 = 0$.

Since 80% of the sandwich beam material is zirconia ceramic at $p = 0$, the maximum phase velocity is 1.95027 km/s, and its associated wave number is $k = 43.98$ (1/nm). As can be seen from the figure, the minimum phase velocity is 1.76306 km/s at $k = 40.8$ (1/nm) wave number at $p = 5$. At $p = 5$, 83% of the core consists of Ti_6Al_4V. $M = 0.6h(0.83) + 0.2(0.5)h_p(2) = 0.698$, which means that 69.8% of the sandwich nanobeam is composed of metal Ti_6Al_4V. In general, the phase velocity increases rapidly up to the wave number $k = 12.56$ (1/nm), after which the increase slows down, and this trend goes up to a maximum and starts to decrease. If it is around $k = 314.018$ (1/nm), it approaches the horizontal limit and does not change for the following wave numbers. The frequency when it reaches this horizontal limit is called the escape frequency, and the speed at which it occurs is called the escape velocity. In Fig. 3(b), wave frequencies increase with increasing ceramic ratio and decrease with increasing metal ratio.

According to the graphs, as the number of waves changes, the phase velocity and frequency change. While the wave frequency increases exponentially according to the wave number, the phase velocity takes its maximum value when the wave number is 45 (1/nm), and the phase velocity decreases after this value. In addition, as the power law index p increases, the phase velocity

and wave frequency decrease. For example, in the region where the phase velocity reaches its maximum value, when the power law index increases from $p=0$ to $p=5$, it is seen that it decreases by 9.7%.

In Fig. 4, the sandwich nanobeam's phase velocity and wave frequency are given for the temperature difference's $\Delta T = 0$, 50, 100, and 150 K values. As mentioned above, at $p=0$, the core part is made of ceramic, and in this case, 80% of the total material of the sandwich nanobeam is made of ceramic. As can be seen from the graphs, the phase velocity decreases with the increase in temperature, and the wave frequency also decreases with the increase in temperature. At $\Delta T = 0$ K, when the wave number is $k=3.14159$ (1/nm), the phase velocity is 0.4594 km/s, and when the wave number is $k=43.98$ (1/nm), the phase velocity reaches its maximum value at 1.991 km/s. If the temperature difference is $\Delta T = 150$ K, the phase velocity is 0.3074 km/s when the wave number is $k=3.14$ (1/nm), and when the wave number is $k=43.98$ (1/nm), the phase velocity reaches its maximum value at 1.844 km/s. Therefore, a temperature increase of 150 K reduces the maximum phase velocity of the sandwich nanobeam by 7.38%. In Fig. 4(b), it is seen that the rise of temperature decreases the wave frequencies for all wave numbers.
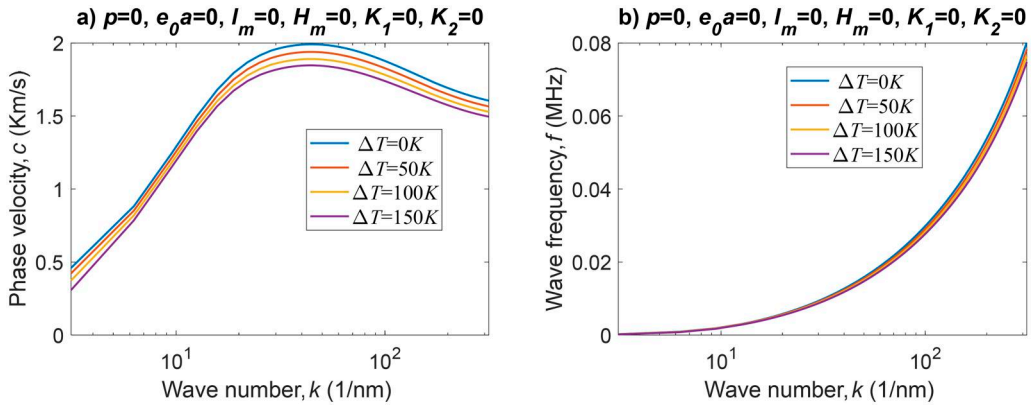

Figure 4. Variation of the phase velocity and wave frequency of the sandwich nanobeam *vs.* wave number k (1/nm) depending on the temperature difference of the sandwich nanobeam for $\Delta T = 0$, 50, 100, 150 K; power law index of FG core $p=0$: full ceramic (zirconia); (a) Phase velocity (km/s); (b) Wave frequency (MHz); $L=100$ nm, $h=L/10$, $b=h$, $h_c=0.6h$, $h_p=0.2h$; Material ratios of faces Ti = 0.5, Zr = 0.5; Ti: Ti$_6$Al$_4$V, Zr:ZrO$_2$; the other parameters: $e_0a=0$, $l_m=0$, $H_m=0$, $K_1=0$, and $K_2=0$.
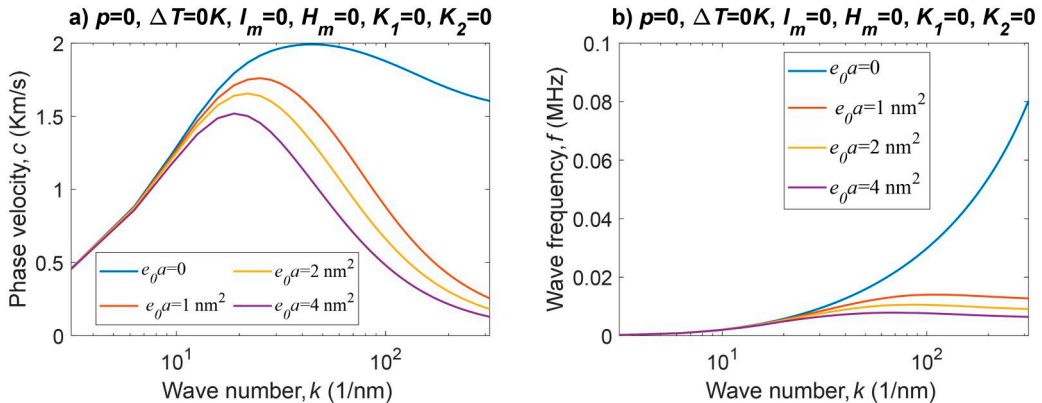

Figure 5. Variation of the phase velocity and wave frequency of the sandwich nanobeam *vs.* wave number k (1/nm) depending on the nonlocal parameter of the sandwich nanobeam core for $e_0a=0$, 1, 2, 4 nm^2; power law index of FG core $p=0$: full ceramic (zirconia); (a) Phase velocity (km/s); (b) Wave frequency (MHz); $L=100$ nm, $h=L/10$, $b=h$, $h_c=0.6h$, $h_p=0.2h$; Material ratios of faces Ti = 0.5, Zr = 0.5; Ti: Ti$_6$Al$_4$V, Zr:ZrO$_2$; the other parameters: $\Delta T=0$, $lm=0$, $Hm=0$, $K_1=0$, and $K_2=0$.

Figure 5 shows the effect of wave number on phase velocity and wave frequency according to four different nonlocal parameters. According to Fig. 5(a), the phase velocity varies with the nonlocal parameter, and its maximum value is 1.98 km/s when $e_0a = 0$ and 1.52 km/s when the nonlocal parameter increases and $e_0a = 4\,nm^2$. In other words, as the nonlocal parameter increases, both the value of the phase velocity and the value of the wave number it occurs decrease. In addition, if the nonlocal parameter is $e_0a = 0$ after the phase velocity takes its maximum value, the rate of decrease of the phase velocity is relatively slow compared to the others. On the other hand, while the wave frequency increases continuously until the wave number reaches 80 in Fig. 5(b), the wave frequency decreases in all nonlocal parameters except $e_0a = 0$. When $e_0a = 0$, the wave frequency increases exponentially. In addition, increasing the nonlocal parameter significantly reduces both the phase velocity and the wave frequency.

Figure 6 shows the phase velocity and wave frequency variation of FG sandwich nanobeam by considering the material size factor. According to the graphs, the phase velocity and wave frequency increase considerably as the material size factor increases. In addition, if the number of waves is 20 or more, phase velocity and wave frequency increase exponentially, except for $l_m = 0$.
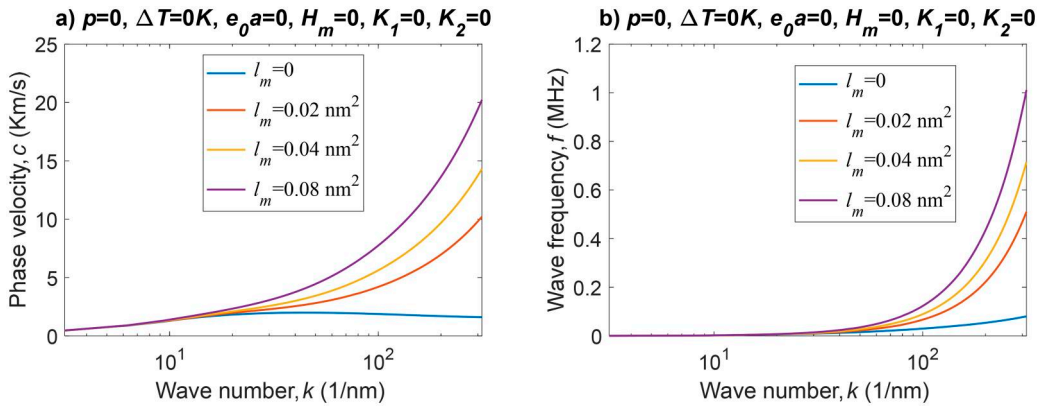

Figure 6. Variation of the phase velocity and wave frequency of the sandwich nanobeam *vs.* wave number k (1/nm) depending on the material size factor of the sandwich nanobeam core for $l_m = 0, 0.02, 0.04, 0.08\,nm^2$; power law index of FG core $p = 0$: full ceramic (zirconia); (a) Phase velocity (km/s); (b) Wave frequency (MHz); $L = 100\,nm$, $h = L/10$, $b = h$, $h_c = 0.6h$, $h_p = 0.2h$; Material ratios of faces Ti = 0.5, Zr = 0.5; Ti: Ti$_6$Al$_4$V, Zr:ZrO$_2$; the other parameters: $\Delta T = 0$, $e_0a = 0$, $H_m = 0$, $K_1 = 0$, and $K_2 = 0$.
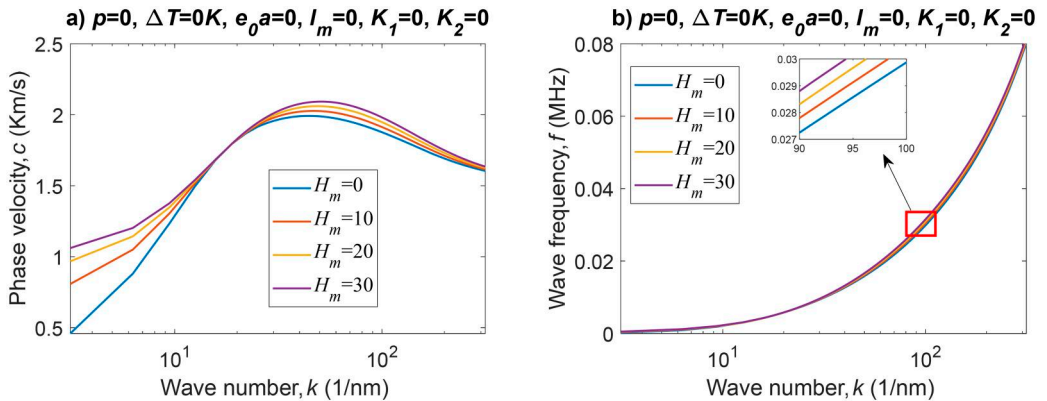

Figure 7. Variation of the phase velocity and wave frequency of the sandwich nanobeam *vs.* wave number k (1/nm) depending on the magnetic field intensity of the sandwich nanobeam core for $H_m = 0, 10, 20, 30$; power law index of FG core $p = 0$: full ceramic (zirconia); (a) Phase velocity (km/s); (b) Wave frequency (MHz); $L = 100\,nm$, $h = L/10$, $b = h$, $h_c = 0.6h$, $h_p = 0.2h$; Material ratios of faces Ti = 0.5, Zr = 0.5; Ti: Ti$_6$Al$_4$V, Zr:ZrO$_2$; the other parameters: $\Delta T = 0$, $e_0a = 0$, $l_m = 0$, $K_1 = 0$, and $K_2 = 0$.
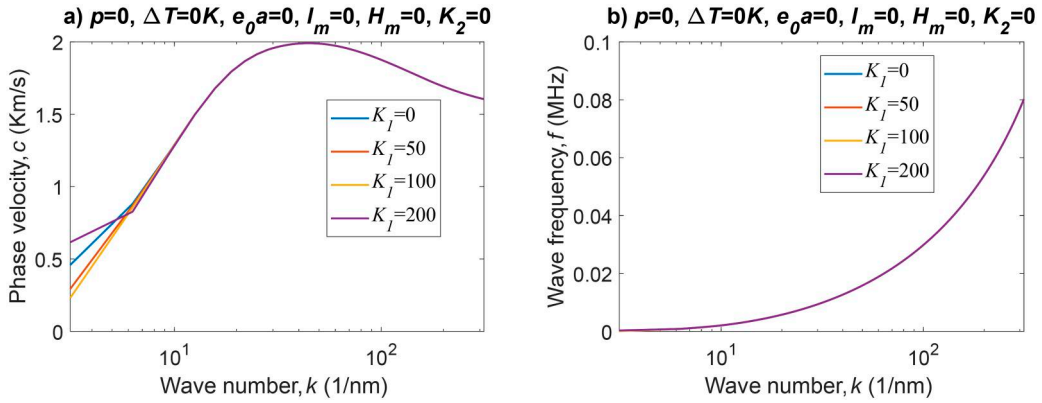
Figure 8. Variation of the phase velocity and wave frequency of the sandwich nanobeam *vs.* wave number k (1/nm) depending on the foundation effect for $K_1 = 0$, 50, 100, 200; power law index of FG core $p = 0$: full seramic (zirconia); (a) Phase velocity (km/s); (b) Wave frequency (MHz); $L = 100$ nm, $h = L/10$, $b = h$, $h_c = 0.6h$, $h_p = 0.2h$; Material ratios of faces Ti = 0.5, Zr = 0.5; Ti: Ti$_6$Al$_4$V, Zr:ZrO$_2$; the other parameters: $\Delta T = 0$, $e_0 a = 0$, $l_m = 0$, and $K_2 = 0$.
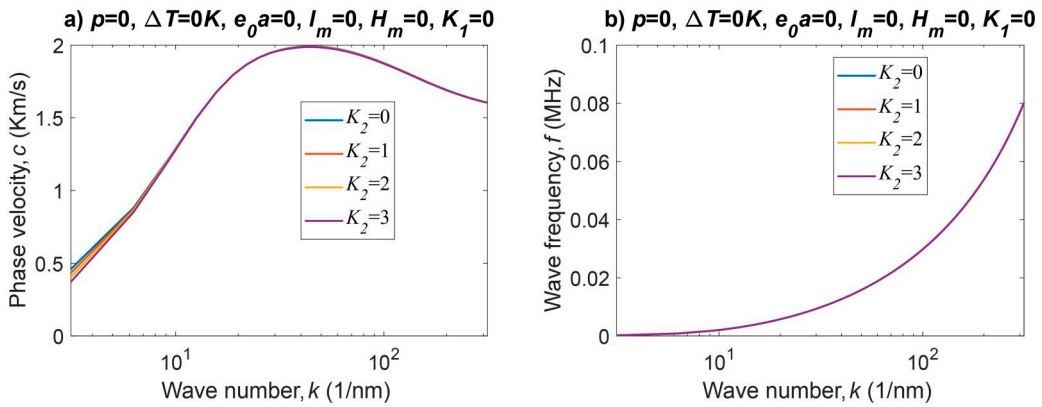

Figure 9. Variation of the phase velocity and wave frequency of the sandwich nanobeam *vs.* wave number k (1/nm) depending on the foundation effect for $K_2 = 0$, 1, 2, 3; power law index of FG core $p = 0$: full ceramic (zirconia); (a) Phase velocity (km/s); (b) Wave frequency (MHz); $L = 100$ nm, $h = L/10$, $b = h$, $h_c = 0.6h$, $h_p = 0.2h$; Material ratios of faces Ti = 0.5, Zr = 0.5; Ti: Ti$_6$Al$_4$V, Zr:ZrO$_2$; the other parameters: $\Delta T = 0$, $e_0 a = 0$, $l_m = 0$, and $K_1 = 0$.

Figure 7 gives the effect of magnetic field intensity on phase velocity and wave frequency of sandwich nanobeam according to wave number. According to Fig. 7(a), increasing the magnetic field intensity increases the phase velocity. However, when the wave number is about 19, the phase velocity is the same regardless of the magnetic field intensity. In addition, the maximum value of the phase velocity occurs when the average number of waves is 50, while the phase velocity decreases after this value. According to Fig. 7(b), while the wave frequency increases as the wave number increases, the increase in the magnetic field partially increases the wave frequency.

In Figs. 8 and 9, the sandwich nanobeam's phase velocity and wave frequency were examined according to the different foundation effects and considering the number of waves. According to the graphics, the maximum value of the phase velocity occurs when the wave number is 44, while the phase velocity and wave frequency are the same in almost the entire foundation coefficient. The wave frequency increases considerably with the increase of the wave number.

In this part, FG nanobeams are considered as four different models, and the phase velocity graphs of these models are examined in detail. The situation where the nanobeam is completely composed of pure zirconium is represented as Model 1, while the situation consisting entirely of pure titanium is represented as Model 2. Model 3, on the other hand, is composed of zirconium
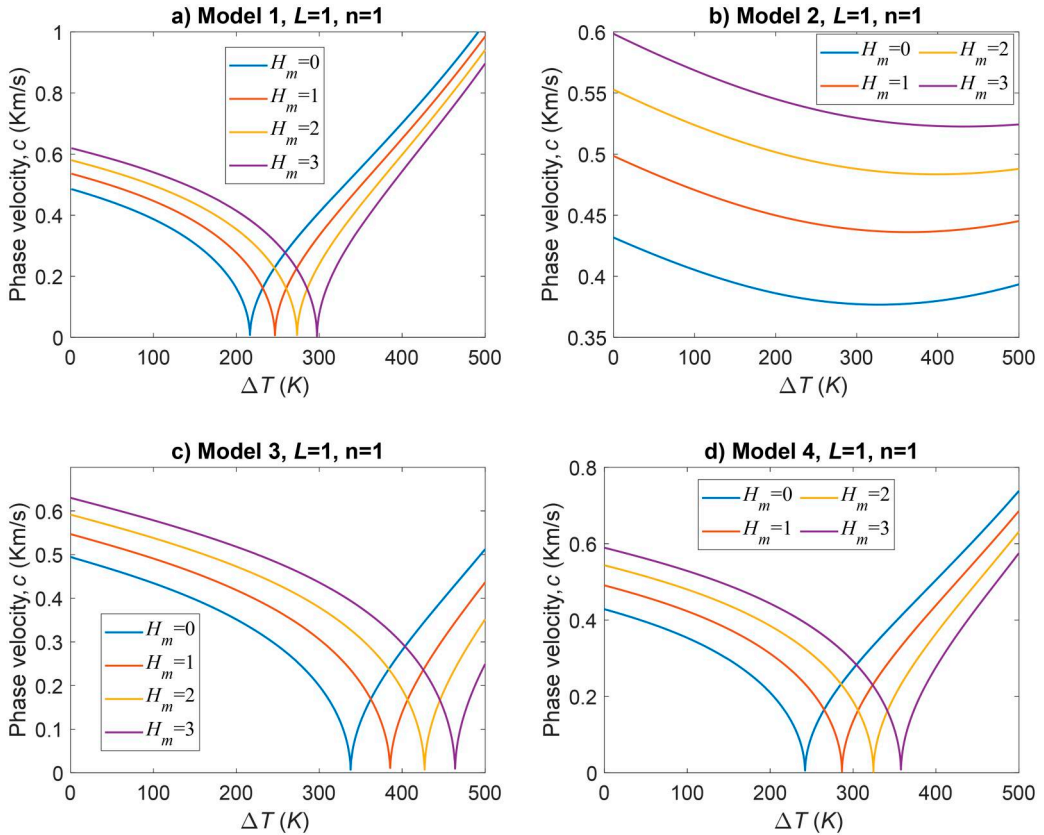
Figure 10. Variation of the phase velocity depending on temperature difference and magnetic field intensity H_m. (a) All of the nanobeam completely %100 zirconium (Model 1:CCC). (b) All of the nanobeam completely %100 titanium (Model 2). (c) The top and bottom of the nanobeam is made entirely of zirconium, while the core is made of titanium (Model 3). (d) The top and bottom of the nanobeam is made entirely of titanium, while the core is made of zirconium (Model 4).

at the top and bottom of the nanobeam and titanium in the middle. Model 4 is composed of titanium at the top and bottom of the nanobeam and zirconium in the middle. In Model 5, the core part is FGM, and the surfaces consist of a mixture of ceramic and metal.

In Fig. 10, the phase velocity variation of four different FG composite nanobeam models is given considering the temperature difference and four different magnetic field intensities, $H_m = 0$, 1, 2, and 3. When the graphs are examined, the phase velocity increases as the magnetic field intensity increases, the phase velocity decreases as the temperature difference increases, and buckling occurs in all models except Model 2. For example, if Model 1 is examined in Fig. 10(a), the phase velocity at $\Delta T = 0$ K is 0.485, 0.536, 0.58, and 0.619 km/s for $H_m = 0$, 1, 2, and 3, respectively. As the temperature increases, the phase velocity drops to zero at 216.4, 246.5, 273.2, and 297.3 K, respectively, and buckling occurs. When Model 2 is examined, the phase velocity at $\Delta T = 0$ K is 0.43, 0.5, 0.55, and 0.6 km/s for $H_m = 0$, 1, 2 and 3, respectively. At $\Delta T = 500$ K, it becomes 0.39, 0.44, 0.49 and 0.52 km/s, respectively. In other words, as the temperature difference increases for Model 2, the phase velocity of the nanobeam decreases by 10% on average. It is also seen in Fig. 10(b) that the phase velocity takes its minimum value at the temperature difference $\Delta T = 350$ K. When Fig. 10(c) is examined, with the increase of magnetic field intensity, buckling occurs by decreasing the phase velocity of the nanobeam to zero at $\Delta T = 337.8$, 385.6, 427, and 463.8 K, respectively. In Fig. 10(d), buckling occurs at $\Delta T = 242.1$, 286.6, 324.5, and 357.8 K, respectively. As a result, as the temperature difference increases, buckling occurs first in Model 1.
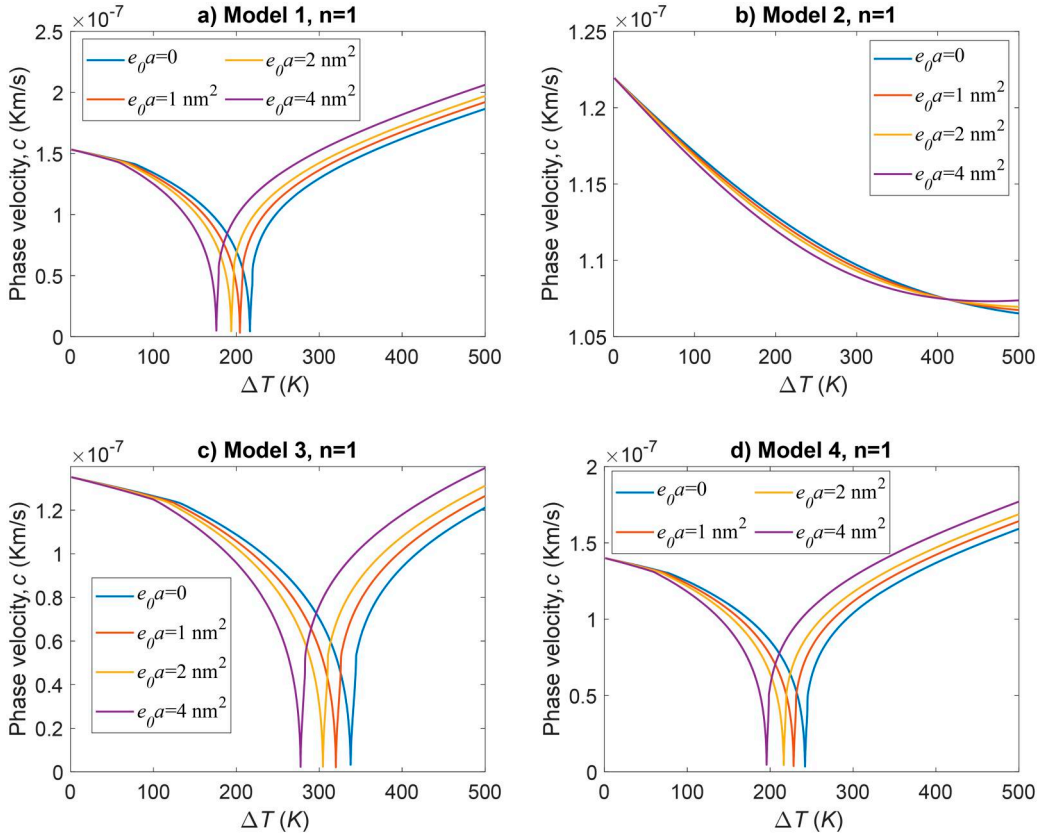
Figure 11. Variation of the phase velocity depending on temperature difference and nonlocal parameter e_0a. (a) All of the nanobeam completely %100 zirconium (Model 1). (b) All of the nanobeam completely %100 titanium (Model 2). (c) The top and bottom of the nanobeam is made entirely of zirconium, while the core is made of titanium (Model 3). (d) The top and bottom of the nanobeam is made entirely of titanium, while the core is made of zirconium (Model 4).

The variation of phase velocity of FG nanobeam with temperature increase is given in Fig. 11, considering four different nonlocal effects and four different Models. When Fig. 11(a) is examined, while the phase velocity is 1.53×10^{-7} km/s for the whole nonlocal effect at temperature difference $\Delta T = 0$, the phase velocity decreases rapidly to zero with the increase of the temperature difference, and buckling occurs. In addition, buckling occurs at lower temperature differences with the increase of nonlocal effect. For example, at $e_0a = 0$, the phase velocity of the nanobeam is buckling at 216.4 K, while at $e_0a = 1$, 2, and 4, the phase velocity decreases to zero at 204.3, 193.8, and 175.8 K, respectively. In Fig. 11(b), the phase velocity change according to the temperature difference of Model 2 is given. In Fig. 11(b), the phase velocity is 1.22×10^{-7} km/s at temperature difference $\Delta T = 0$, while the phase velocity decreases as the temperature difference increases and becomes 1.65×10^{-7} km/s at $\Delta T = 500$. In this graph, as the nonlocal effect increases, the rate of decrease of the phase velocity increases partially up to $\Delta T = 400$ K, while the increase of the nonlocal effect decreases the rate of decrease of the phase velocity after this temperature difference. In Fig. 11(c), when the phase velocity of Model 3 is examined according to the temperature change, it is seen that with the increase of the temperature difference, buckling occurs first in cases where the nonlocal effect is high. Similarly, buckling occurs at lower temperature differences with the increase of the nonlocal effect in Fig. 11(d).

In Fig. 12, the effect of four different material size factors on the phase velocity of the nanobeam is given by considering the temperature difference and four different models. When the graphs are
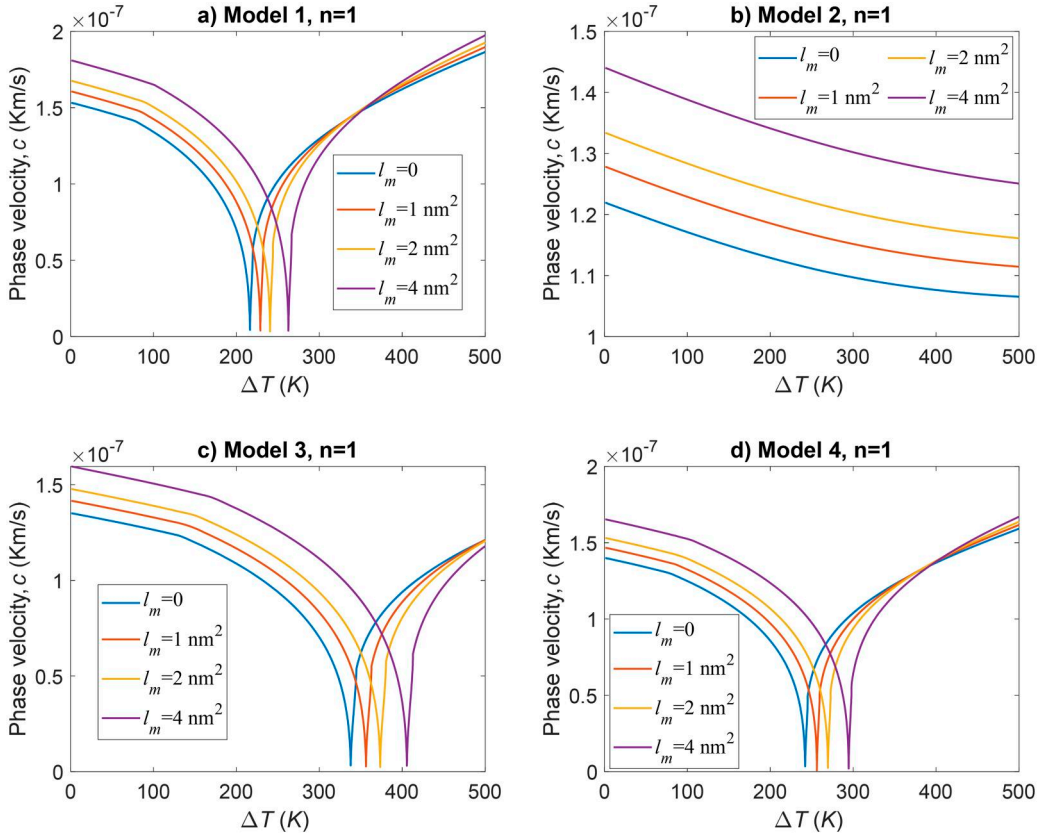
Figure 12. Variation of the phase velocity depending on temperature difference and material size factor l_m. (a) All of the nanobeam completely %100 zirconium (Model 1). (b) All of the nanobeam completely %100 titanium (Model 2). (c) The top and bottom of the nanobeam is made entirely of zirconium, while the core is made of titanium (Model 3). (d) The top and bottom of the nanobeam are made entirely of titanium, while the core is made of zirconium (Model 4).

examined, the phase velocity decreases as the temperature difference increases, while the phase velocity increases as the material size factor increases. For example, at $\Delta T = 0$ K and $l_m = 0$, the phase velocity of the nanobeam is 1.53×10^{-7}, 1.22×10^{-7}, 1.35×10^{-7}, and 1.4×10^{-7} km/s for Model 1,2,3, and 4, respectively. When $l_m = 4$, it becomes 1.81×10^{-7}, 1.44×10^{-7}, 1.6×10^{-7}, and 1.65×10^{-7} km/s, respectively. In other words, an increase in the material size factor increases the phase velocity by 18% on average. In addition, the rise in the material size factor also increases the temperature difference required for the buckling of the nanobeam. For example, when Fig. 12(a) is examined, with the increase of l_m, the phase velocity of the nanobeam decreases to zero at 216.4, 228.9, 240.6, and 262.7 K, respectively, and buckling occurs. Similarly, buckling occurs in other models as the temperature difference increases, while in Model 3, the temperature difference at which the nanobeam is buckling is the highest.

Figure 13 investigated the phase velocity of the nanobeam considering the effect of FG composite nanobeam thickness and varying temperature differences. Here, nanobeam thickness was investigated in four different thicknesses: $h = L/10$, $h = L/25$, $h = L/50$, and $h = L/100$. According to the graphs, the nanobeam thickness does not significantly affect the phase velocity. However, only in Model 2, the phase velocity increases as the thickness increases. In addition, as the temperature difference increases, the phase velocity decreases, and buckling occurs at ~220, 340, and 245 K values for Model 1, Model 3, and Model 4, respectively. In this case, if the nanobeam consisted entirely of titanium, buckling did not occur with the increase of the temperature difference.
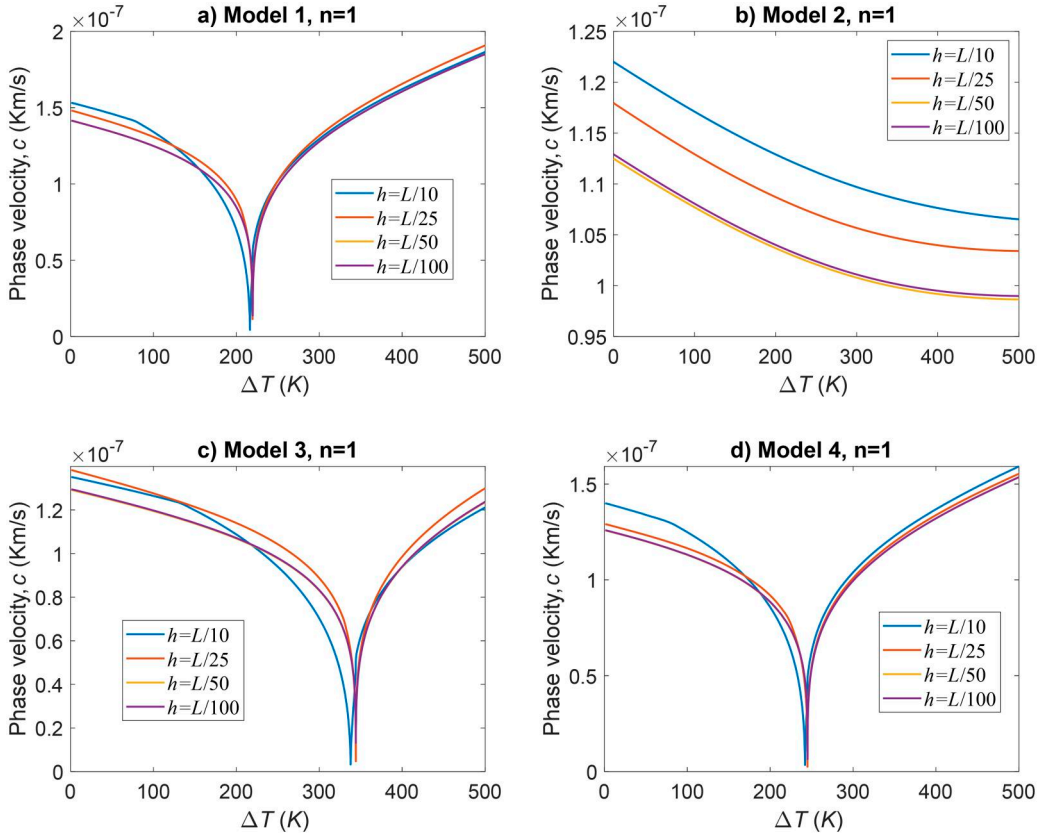
Figure 13. Variation of the phase velocity depending on temperature difference and nanobeam thickness h. (a) All of the nanobeam completely %100 zirconium (Model 1). (b) All of the nanobeam completely %100 titanium (Model 2). (c) The top and bottom of the nanobeam is made entirely of zirconium, while the core is made of titanium (Model 3). (d) The top and bottom of the nanobeam is made entirely of titanium, while the core is made of zirconium (Model 4).

In Fig. 14, the phase velocity of the FG nanobeam was examined by considering the temperature change and three different core thicknesses as $h_c/h = 0.4$, $h_c/h = 0.6$, $h_c/h = 0.8$. According to the graphs, the increase in the thickness of the core increases the phase velocity, while it decreases as the temperature difference increases. In addition, it can be seen from other graphics, except Model 2, that buckling occurs as the temperature difference increases. For example, in Fig. 14(a), buckling occurs at 164.3, 216.4, and 266.2 K for $h_c/h = 0.4$, $h_c/h = 0.6$, $h_c/h = 0.8$, respectively, while these values are 235.4, 337.8, and 266.2 K for Model 3. For Model 4, they are 197.1, 242.1, and 287.6 K, respectively. When Fig. 14(b) is examined, the phase velocity of the nanobeam for $\Delta T = 0$ K and $h_c/h = 0.4$, $h_c/h = 0.6$, $h_c/h = 0.8$ is 1.04×10^{-7}, 1.22×10^{-7}, and 1.37×10^{-7} km/s, respectively. When the temperature difference is $\Delta T = 500$ K, these values are 0.92×10^{-7}, 1.06×10^{-7}, and 1.19×10^{-7} km/s, respectively. In this case, the phase velocity of the nanobeam decreases by an average of 12–13% with the increase of the temperature difference for Model 2.

In Fig. 15, the phase velocity of an FG sandwich nanobeam is given by considering the fundamental wave $n = 1$ and $n = 14$ wave numbers and their variation according to four different magnetic field intensities and temperature differences. In Fig. 15(a), the $n = 1$ phase velocity of the fundamental wave decreases as the temperature difference increases. For example, when $\Delta T = 0$, the phase velocity of the nanobeam becomes 0.46, 0.51, 0.56, and 0.61 km/s, respectively, according to the magnetic field intensity $H_m = 0$, 1, 2, and 3. In Fig. 15(b), if $n = 14$ and the temperature
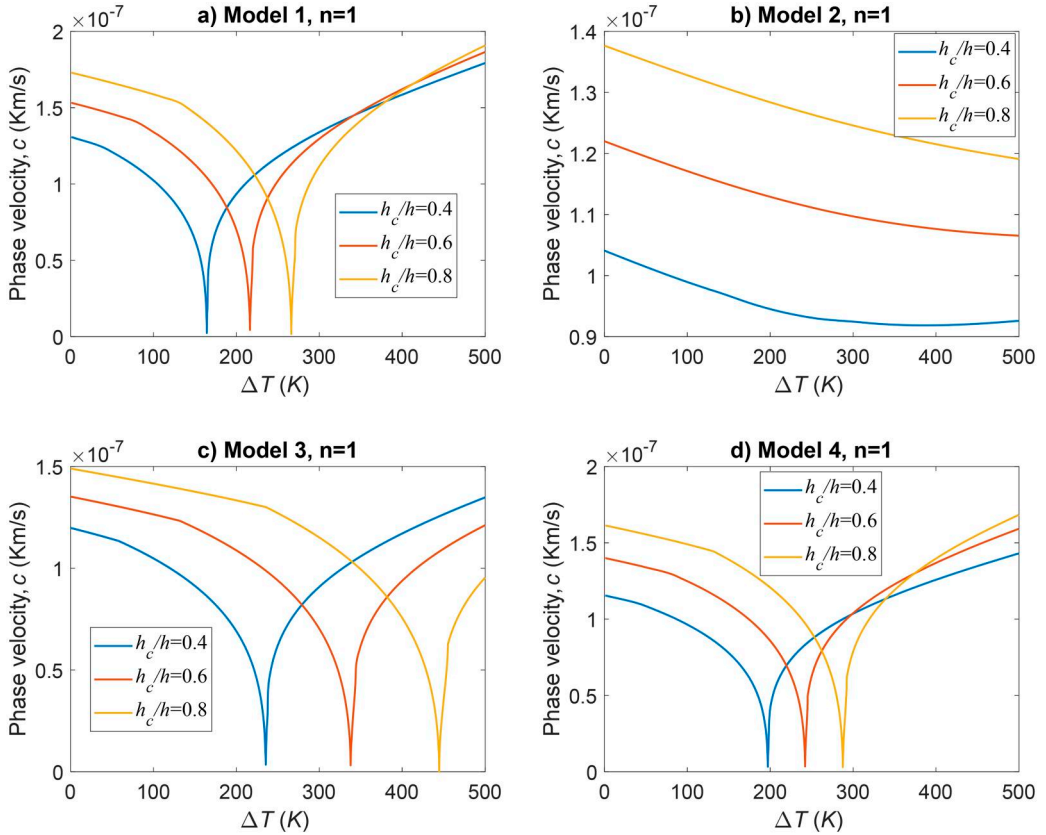
Figure 14. The variation of the phase velocity depending on the core thickness ratio $h_c/h = 0.4, 0.6, 0.8$, and temperature difference. (a) All of the nanobeam completely %100 zirconium (Model 1). (b) All of the nanobeam completely %100 titanium (Model 2). (c) The top and bottom of the nanobeam is made entirely of zirconium, while the core is made of titanium (Model 3). (d) The top and bottom of the nanobeam is made entirely of titanium, while the core is made of zirconium (Model 4).
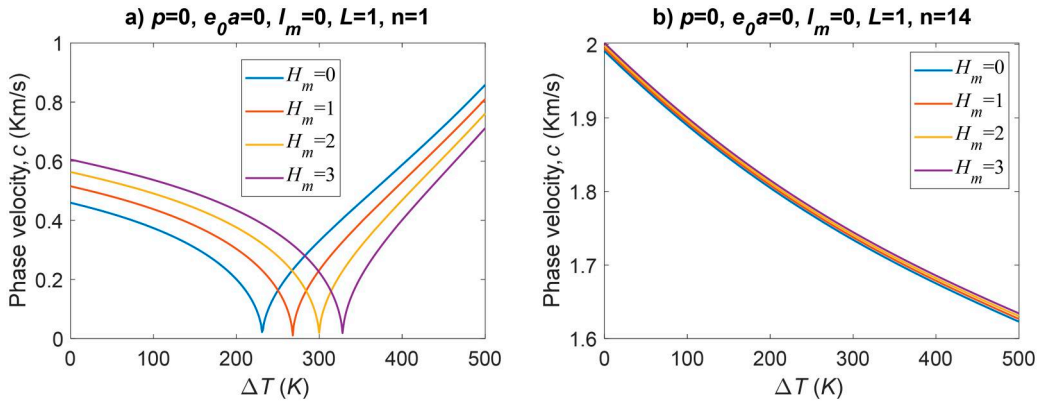

Figure 15. Variation of the phase velocity of the sandwich nanobeam *vs.* temperature difference ΔT (K) depending on the magnetic field intensity for $H_m = 0, 1, 2, 3$. (a) Fundamental wave number $n = 1$. (b) Wave number $n = 14$; $L = 100$ nm, $h = L/10$, $b = h$, $h_c = 0.6h$, $h_p = 0.2h$; Material ratios of faces Ti = 0.5, Zr = 0.5; Ti: Ti$_6$Al$_4$V, Zr:ZrO$_2$.

difference is $\Delta T = 0$, the phase velocity decreases from an average of 2 km/s to an average of 1.63 km/s when $\Delta T = 500$ K.

In Fig. 16, the phase velocity of the nanobeam is given according to two different wave numbers in case the power law index changes between $p = 0$–5 and exposed to four different magnetic field intensities. In Fig. 16(a), as the power law index p and magnetic field intensity H_m increase, the phase velocity of the FG sandwich nanobeam increases. For example, if $H_m = 0$, 1, 2, and 3 at $p = 0$, the phase velocity is 0.459, 0.515, 0.564, and 0.606 km/s, respectively. If the power law index was $p = 5$, that is, 83.3% of the core was composed of Ti$_6$Al$_4$V, these values were 0.467, 0.524, 0.572, and 0.614 km/h, respectively. In other words, with the increase of the power law index, the phase velocity increases by 1.5% on average, while the increase in the magnetic field intensity increases the phase velocity by about 20%. In Fig. 16(b), if $n = 14$, the phase velocity of the nanobeam decreases logarithmically as the power law index increases.

In Fig. 17, the phase velocity variation of the sandwich nanobeam is given by considering the four different material size factors and temperature variation. According to the graph, if the number of fundamental waves is $n = 1$, the phase velocity decreases, and buckling occurs as the temperature difference increases, while if the wave number is $n = 14$, the increase in the temperature difference partially reduces the phase velocity. In Fig. 17(a), buckling occurs between $\Delta T = 245$–280 K of the temperature difference according to the material size factor.
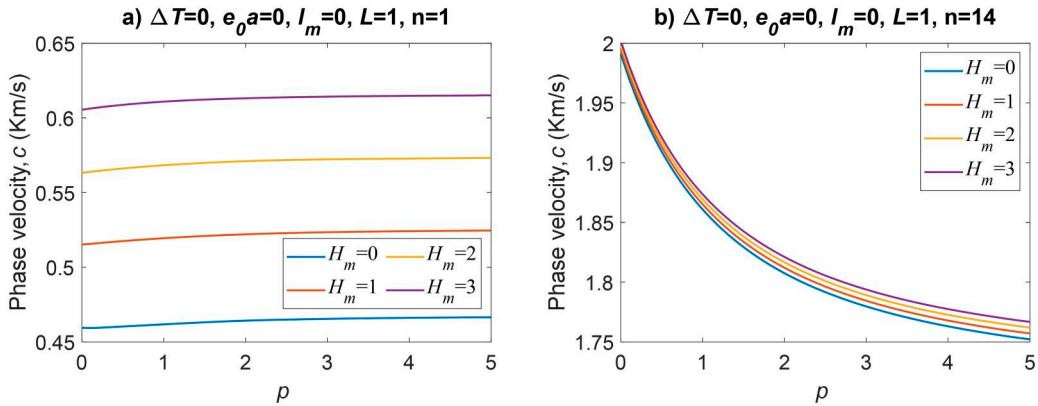

Figure 16. Variation of the phase velocity of the sandwich nanobeam *vs.* power law index depending on the magnetic field intensity for $H_m = 0$, 1, 2, 3. (a) Fundamental wave number $n = 1$. (b) Wave number $n = 14$; $L = 100$ nm, $h = L/10$, $b = h$, $h_c = 0.6h$, $h_p = 0.2h$; Material ratios of faces Ti $= 0.5$, Zr $= 0.5$; Ti: Ti$_6$Al$_4$V, Zr:ZrO$_2$.
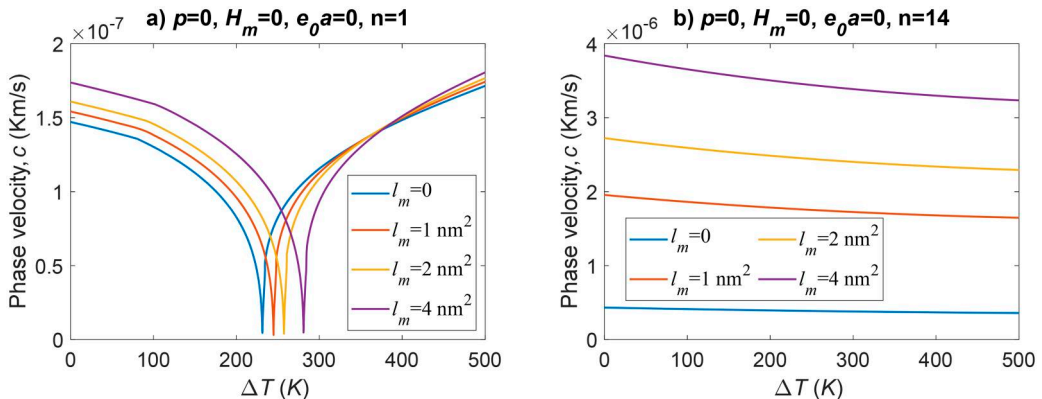

Figure 17. Variation of the phase velocity of the sandwich nanobeam *vs.* temperature difference ΔT (K) depending on the material size factor for $l_m = 0$, 1, 2, 4. (a) Fundamental wave number $n = 1$. (b) Wave number $n = 14$; $L = 100$ nm, $h = L/10$, $b = h$, $h_c = 0.6h$, $h_p = 0.2h$; Material ratios of faces Ti $= 0.5$, Zr $= 0.5$; Ti: Ti$_6$Al$_4$V, Zr:ZrO$_2$.

In Fig. 18, the phase velocity graphs of FG sandwich nanobeams are given considering the power law index varying between $p = 0$–5 and four different material size factors. Phase velocity decreases as the power law index and material size factor decrease in all graphs. For example, when $p = 0$ and $l_m = 0$, 1, 2, and $4\,nm^2$ in Fig. 18(a), the phase frequency becomes 1.47×10^{-7}, 1.54×10^{-7}, 1.61×10^{-7}, and $1.74 \times 10^{-7}\,km/s$, respectively, while When $p = 5$, the phase frequency of the nanobeam is 1.32×10^{-7}, 1.38×10^{-7}, 1.44×10^{-7}, and $1.56 \times 10^{-7}\,km/s$, respectively. In this case, the core part of the nanobeam consists entirely of ceramic, and the phase velocity in the fundamental wave number of the nanobeam decreases by about 10% with the increase of the metal ratio, that is, the increase in the power law index. In Fig. 18(b), when $n = 14$, $p = 0$ and $l_m = 0$, 1, 2, and $4\,nm^2$, the phase velocity of the nanobeam is 4.3×10^{-7}, 19.55×10^{-7}, 27.24×10^{-7}, and $38.39 \times 10^{-7}\,km/s$, respectively. and when $p = 5$, it becomes 3.72×10^{-7}, 16.82×10^{-7}, 23.43×10^{-7}, and $33.01 \times 10^{-7}\,km/h$, respectively.

The change of phase velocity depending on the temperature of the sandwich nanobeam is examined in Fig. 19 by considering four different slenderness ratios. When the graphs are examined, when $n = 1$ fundamental wave number, phase velocity decreases rapidly with the increase in temperature difference, and buckling occurs at $\sim$235 K, regardless of the value of the slenderness
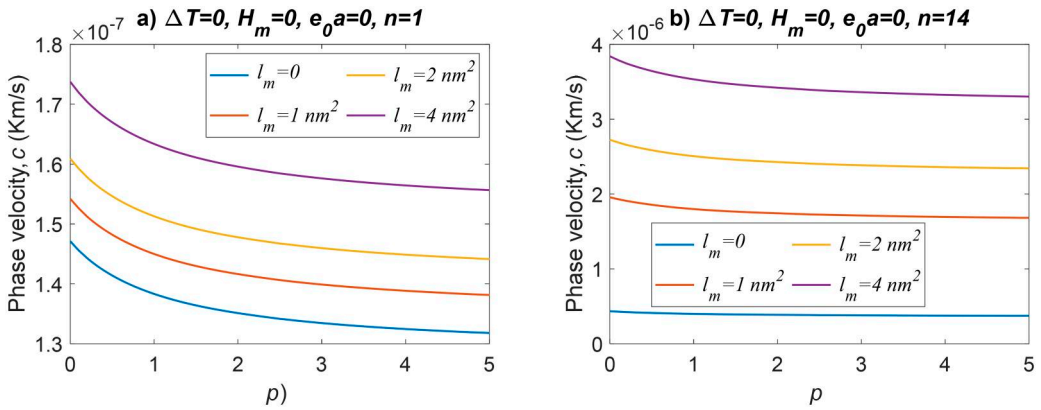

Figure 18. Variation of the phase velocity of the sandwich nanobeam power law index p depending on the material size factor for $l_m = 0$, 1, 2, 4. (a) Fundamental wave number $n = 1$. (b) Wave number $n = 14$; $L = 100\,nm$, $h = L/10$, $b = h$, $h_c = 0.6h$, $h_p = 0.2h$; Material ratios of faces Ti $= 0.5$, Zr $= 0.5$; Ti: Ti$_6$Al$_4$V, Zr:ZrO$_2$.
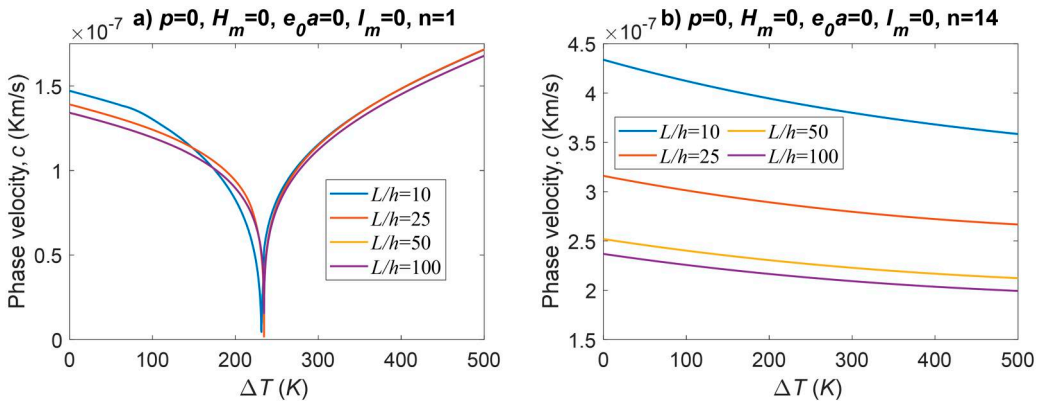

Figure 19. Variation of the phase velocity of the sandwich nanobeam temperature difference ΔT (K) depending on the slenderness ratio for $L/h = 10$, 25, 50, 100. (a) Fundamental wave number $n = 1$. (b) Wave number $n = 14$; $L = 100\,nm$, $h = L/10$, $b = h$, $h_c = 0.6h$, $h_p = 0.2h$; Material ratios of faces Ti $= 0.5$, Zr $= 0.5$; Ti: Ti$_6$Al$_4$V, Zr:ZrO$_2$.

ratio. If the wave number is $n = 14$, phase velocity decreases as the temperature difference and slenderness ratio increase. For example, in Fig. 19(b), while the phase velocity of sandwich nanobeam is 4.34×10^{-7} km/s at slenderness ratio $L/h = 10$ and $\Delta T = 0$ K when the temperature difference is $\Delta T = 500$ K, it decreases by 17.5% and becomes 3.58×10^{-7} km/s. In the same case, if the slenderness ratio is $L/h = 100$, the phase velocity decreases from 2.37×10^{-7} to 1.99×10^{-7} km/s.

In Fig. 20, the effect of four different slenderness ratios on phase velocity was investigated by considering the power law index showing the material component of the FG core of the sandwich nanobeam. According to the graphs, with the increase of the power law index, the ceramic ratio of the core part of the sandwich nanobeam decreases, and the metal ratio increases, in this case, the phase velocity decreases almost at a similar rate. When Fig. 20(a) is examined, if the slenderness ratio is $L/h = 25$, the phase velocity is 1.39×10^{-7} km/s at $p = 0$ and 1.3×10^{-7} km/s at $p = 5$. In other words, as the ceramic ratio of the nanobeam core decreases from 100 to 17%, the phase velocity decreases by 6.47%. In addition, the slenderness ratio, which shows the ratio of the length and thickness of the sandwich nanobeam, also affects the phase velocity. For example, in Fig. 20(a), when $L/h = 10$, phase velocity is 1.47×10^{-7} km/s, and when $L/h = 50$, it decreases 8.8% to 1.34×10^{-7} km/s. In addition, if the slenderness ratio is $L/h = 50$ and $L/h = 100$ in this graph, the phase velocity of the nanobeam is the same, while it is different in Fig. 20(b). Because, in Fig.
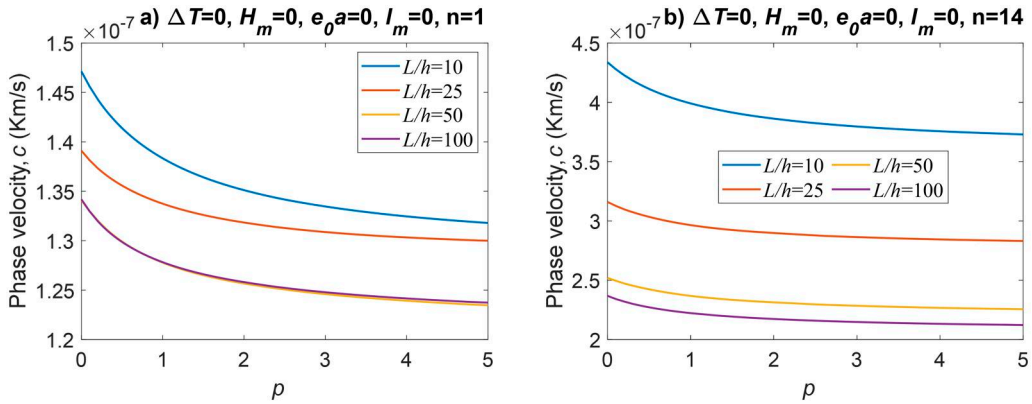

Figure 20. Variation of the phase velocity of the sandwich nanobeam power law index p depending on the slenderness ratio for $L/h = 10, 25, 50, 100$. (a) Fundamental wave number $n = 1$. (b) Wave number $n = 14$; $L = 100$ nm, $h = L/10$, $b = h$, $h_c = 0.6h$, $h_p = 0.2h$; Material ratios of faces Ti $= 0.5$, Zr $= 0.5$; Ti: Ti$_6$Al$_4$V, Zr:ZrO$_2$.
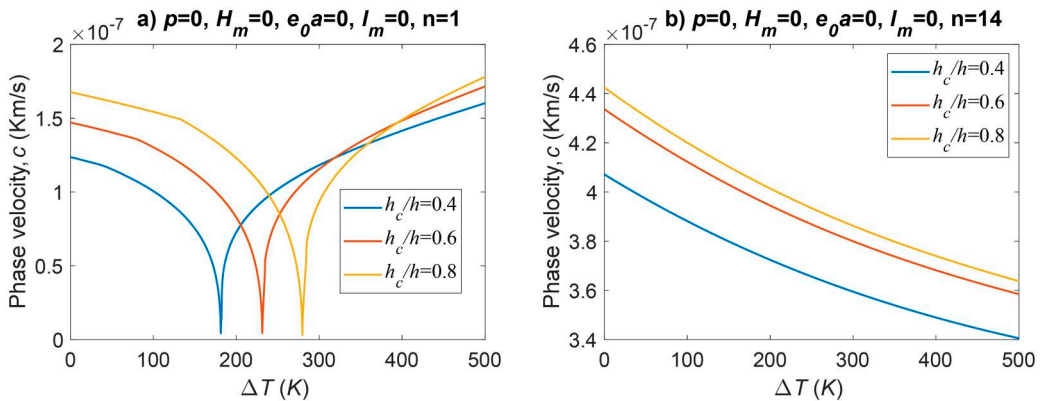
Figure 21. Variation of the phase velocity of the sandwich nanobeam temperature difference ΔT (K) depending on the thickness of beam core for $h_c/h = 0.4, 0.6, 0.8$. (a) Fundamental wave number $n = 1$. (b) Wave number $n = 14$; $L = 100$ nm, $h = L/10$, $b = h$, $h_c = 0.6h$, $h_p = 0.2h$; Material ratios of faces Ti $= 0.5$, Zr $= 0.5$; Ti: Ti$_6$Al$_4$V, Zr:ZrO$_2$.

Figure 22. Variation of the phase velocity of the sandwich nanobeam power law index p depending on the thickness of beam core for $h_c/h = 0.4, 0.6, 0.8$. (a) Fundamental wave number $n = 1$. (b) Wave number $n = 14$; $L = 100$ nm, $h = L/10$, $b = h$, $h_c = 0.6h$, $h_p = 0.2h$; Material ratios of faces Ti = 0.5, Zr = 0.5; Ti: Ti$_6$Al$_4$V, Zr:ZrO$_2$.
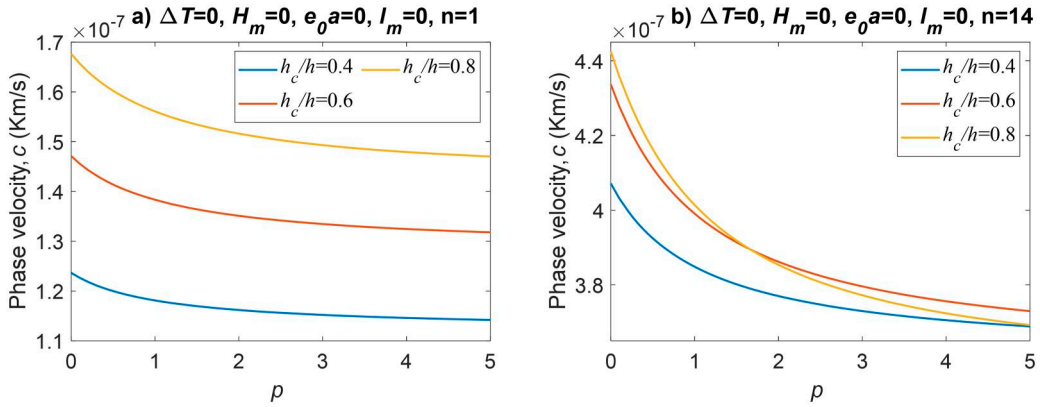
20(b), the wave number is $n = 14$. If the number of waves increases from $n = 1$ to $n = 14$, the phase velocities increase approximately three times.

The effect of temperature change in Fig. 21 on the phase velocity of the nanobeam was investigated by considering the ratio of the core part of the nanobeam to the beam thickness. The thickness ratio of the core of the sandwich nanobeam was examined in three different thicknesses: $h_c/h = 0.4$, $h_c/h = 0.6$, and $h_c/h = 0.8$. When the graphs are examined, as the temperature difference increases, the phase velocity of the sandwich nanobeam decreases considerably. However, one thing to consider here is the number of waves. When the number of waves is $n = 1$, buckling occurs when the temperature difference increases, while the number of waves is $n = 14$, buckling does not occur, only the phase velocity decreases. For example, when the thickness of the core is $h_c/h = 0.4$, $h_c/h = 0.6$, and $h_c/h = 0.8$, buckling occurs if the temperature difference is $\Delta T = 181.3$ K, $\Delta T = 231.4$ K, and $\Delta T = 279.7$ K, respectively. In this case, with the increase in the thickness of the core, both the buckling formation temperature and the phase velocity of the nanobeam increase. For example, in Fig. 21(b), if the temperature difference is $\Delta T = 0$ K and the thickness of the core is $h_c/h = 0.4$, $h_c/h = 0.6$ and $h_c/h = 0.8$, the phase velocity of the sandwich nanobeam is 4.07×10^{-7} km/s, 4.34×10^{-7} and 4.42×10^{-7} km/h, when the temperature difference is $\Delta T = 500$ K, it becomes 3.4×10^{-7}, 3.58×10^{-7}, and 3.64×10^{-7} km/s, respectively. In this case, when the wave number is $n = 14$, the phase velocity of the sandwich nanobeam decreases by about 17% as the temperature difference increases.

In Fig. 22, the effect of the power law index varying in the range of $p = 0$–5 on the phase velocity of the sandwich nanobeam was investigated by considering the thickness of the nanobeam core. As can be seen in these graphs, as the thickness of the core of the nanobeam increases, the phase velocity increases, while the power law index decreases as p increases. However, when the wave number is $n = 14$, and the power law index is $p = 5$, the graphs of both the phase velocity values of the nanobeam are quite close to each other. When $n = 1$ this situation is different.

6. Conclusion

The present study examines the characteristics of free vibration and thermal buckling in sandwich structures composed of FGMs with embedded nanobeams. These structures are subjected to both magnetic and thermal fields. The study focuses on examining the impact of material composition and nonlinear temperature rise on the effective material properties (modulus of elasticity,

Poisson's ratio, thermal expansion, and conductivity coefficients) of the FGM sandwich-embedded nanobeam. Furthermore, this study examines the impact of the power law index, material size factor, and material distribution functions on the nonlinear temperature and stress distributions across the nanobeam's thickness. The analysis takes into account a bottom surface temperature of $T_b = 300$ K and the application of a temperature difference of $\Delta T = 300$ K. Subsequently, the motion equations for the free vibration response of the nanobeam are derived by employing the trigonometric higher-order shear deformation theory, which incorporates the micromechanical influences of nonlocal differential elasticity and strain gradient elasticity. The study extensively models and investigates the impact of nonlocal parameters, nonlinear temperature, magnetic field intensities, and material distribution function on the free vibration behavior of the sandwich embedded nanobeam. In conclusion, the findings derived from the analyses are succinctly presented as follows.

- The phase velocity exhibits a rapid increase until reaching a wave number of $k = 12.56$ (1/nm), beyond which the rate of increase diminishes. This trend continues until reaching a maximum value, after which the phase velocity decreases.
- As wave number varies, phase velocity and frequency vary. While the wave frequency grows exponentially with wave number, the phase velocity peaks at 45 (1/nm) and drops thereafter.
- The sandwich nanobeam's core is formed of ceramic at $p = 0$, making up 80% of its material. The plots indicate that phase velocity and wave frequency drop when temperature rises.
- The phase velocity exhibits variation about the nonlocal parameter, with a maximum value of 1.98 km/s observed when e_0a equals zero. As the nonlocal parameter increases and e_0a reaches 4 nm^2, the phase velocity decreases to 1.52 km/s.
- The phase velocity exhibits a positive correlation with the magnetic field intensity, while it demonstrates a negative correlation with the temperature difference. Additionally, buckling is observed in all models except for Model 2 (MMM).
- The phase velocity for the entire nonlocal effect is 1.53×10^{-7} km/s when the temperature difference $\Delta T = 0$. As the temperature difference increases, the phase velocity decreases rapidly and eventually reaches zero, leading to buckling.
- An augmentation in the material size factor results in an average 18% increase in the phase velocity. Furthermore, the increase in the size of the material also leads to an augmentation in the temperature differential necessary for the buckling phenomenon to occur in the nanobeam.
- Variations do not significantly influence the phase velocity in the thickness of the sandwich nanobeam. However, it is only in Model 2 (MMM) where the phase velocity exhibits an increase with an increase in thickness.
- The phase velocity is positively correlated with the increase in core thickness but negatively correlated with the increase in temperature difference. Furthermore, it is evident from alternative graphics, apart from Model 2, that buckling transpires with the augmentation of temperature disparity.
- Functionally graded sandwich nanobeam phase velocity grows with a power law index p and magnetic field strength H_m. For example, $H_m = 0$, 1, 2, and 3 at $p = 0$ have phase velocities of 0.459, 0.515, 0.564, and 0.606 km/s. If the power law index was $p = 5$, meaning 83.3% of the core was Ti$_6$Al$_4$V, these values were 0.467, 0.524, 0.572, and 0.614 km/h.
- If the central component of the nanobeam is composed exclusively of ceramic material. The phase velocity at the fundamental wave number of the nanobeam exhibits a decrease of ~10% as the metal ratio increases, i.e., as the power law index increases.
- The phase velocity of the sandwich nanobeam decreases with an increase in both the slenderness ratio and power law index. Furthermore, when the slenderness ratio is $L/h = 25$, the phase

velocity is 1.39×10^{-7} Km/s at $p = 0$ and 1.3×10^{-7} km/s at $p = 5$. To clarify, when the ceramic ratio of the nanobeam core is reduced from 100 to 17%, there is a corresponding decrease in the phase velocity by 6.47%.

- The investigation focused on three distinct thickness ratios (h_c/h) of the core in the sandwich nanobeam: 0.4, 0.6, and 0.8. When the number of waves is $n = 1$, buckling phenomena manifest as the temperature difference increases. Conversely, when the number of waves is $n = 14$, buckling does not occur. However, it is observed that both the phase velocity and wave frequency experience a decrease. In the given scenario, buckling is observed at different temperature differences, ΔT, when the ratio of the core thickness, h_c, to the total thickness, h, is 0.4, 0.6, and 0.8. Specifically, buckling occurs at ΔT values of 181.3, 231.4, and 279.7 K, respectively.

Disclosure statement

No potential conflict of interest was reported by the author(s).

ORCID

Mustafa Eroğlu ⬤ http://orcid.org/0000-0002-1429-7656
İsmail Esen ⬤ http://orcid.org/0000-0002-7853-1464
Mehmet Akif Koç ⬤ http://orcid.org/0000-0001-7461-9795

References

Al-Furjan, M. S. H., M. X. Xu, A. Farrokhian, G. S. Jafari, X. Shen, and R. Kolahchi. 2022. "On Wave Propagation in Piezoelectric-Auxetic Honeycomb-2D-FGM Micro-Sandwich Beams Based on Modified Couple Stress and Refined Zigzag Theories." *Waves in Random and Complex Media* 1–25. https://doi.org/10.1080/17455030.2022.2030499

Al-Furjan, M. S. H., S. Fan, L. Shan, A. Farrokhian, X. Shen, and R. Kolahchi. 2023. "Wave Propagation Analysis of Micro Air Vehicle Wings with Honeycomb Core Covered by Porous FGM and Nanocomposite Magnetostrictive Layers." *Waves in Random and Complex Media* 1–30. https://doi.org/10.1080/17455030.2022.2164378

Al-Osta, M. A. 2023. "An Efficient Model for Wave Propagation of Temperature-Dependent E-FGM Plates Resting on Viscoelastic Foundation." *Materials Today Communications* 35: 105784. https://doi.org/10.1016/j.mtcomm.2023.105784

Arani, A. G., and M. H. Jalaei. 2017. "Investigation of the Longitudinal Magnetic Field Effect on Dynamic Response of Viscoelastic Graphene Sheet Based on Sinusoidal Shear Deformation Theory." *Physica B: Condensed Matter* 506: 94–104. https://doi.org/10.1016/j.physb.2016.11.004

Askes, H., and E. C. Aifantis. 2009. "Gradient Elasticity and Flexural Wave Dispersion in Carbon Nanotubes." *Physical Review B* 80 (19): 195412. https://doi.org/10.1103/PhysRevB.80.195412

Avcar, M., L. Hadji, and Ö. Civalek. 2021. "Natural Frequency Analysis of Sigmoid Functionally Graded Sandwich Beams in the Framework of High Order Shear Deformation Theory." *Composite Structures* 276: 114564. https://doi.org/10.1016/j.compstruct.2021.114564

Belarbi, M. O., A. Garg, M. S. A. Houari, H. Hirane, A. Tounsi, and H. D. Chalak. 2022. "A Three-Unknown Refined Shear Beam Element Model for Buckling Analysis of Functionally Graded Curved Sandwich Beams." *Engineering with Computers* 38 (S5): 4273–4300. https://doi.org/10.1007/s00366-021-01452-1

Belarbi, M. O., M. S. A. Houari, H. Hirane, A. A. Daikh, and S. P. A. Bordas. 2022. "On the Finite Element Analysis of Functionally Graded Sandwich Curved Beams via a New Refined Higher Order Shear Deformation Theory." *Composite Structures* 279: 114715. https://doi.org/10.1016/j.compstruct.2021.114715

Bui, X. B., T. K. Nguyen, and P. T. T. Nguyen. 2023. "Stochastic Vibration and Buckling Analysis of Functionally Graded Sandwich Thin-Walled Beams." *Mechanics Based Design of Structures and Machines* 1–23. https://doi.org/10.1080/15397734.2023.2165101

Burlayenko, V. N., T. Sadowski, and H. Altenbach. 2022. "Efficient Free Vibration Analysis of FGM Sandwich Flat Panels with Conventional Shell Elements." *Mechanics of Advanced Materials and Structures* 29 (25): 3709–3726. https://doi.org/10.1080/15376494.2021.1909191

Chaabani, H., S. Mesmoudi, L. Boutahar, and K. El Bikri. 2023. "A High-Order Finite Element Continuation for Buckling Analysis of Porous FGM Plates." *Engineering Structures* 279: 115597. https://doi.org/10.1016/j.engstruct.2023.115597

Chami, G. M. B., A. Kahil, and L. Hadji. 2022. "Influence of Porosity on the Fundamental Natural Frequencies of FG Sandwich Beams." *Materials Today: Proceedings* 53: 107–112. https://doi.org/10.1016/j.matpr.2021.12.404

Chan, D. Q., T. Q. Quan, B. G. Phi, D. Van Hieu, and N. D. Duc. 2022. "Buckling Analysis and Dynamic Response of FGM Sandwich Cylindrical Panels in Thermal Environments Using Nonlocal Strain Gradient Theory." *Acta Mechanica* 233 (6): 2213–2235. https://doi.org/10.1007/s00707-022-03212-8

Chedad, A., N. Elmeiche, S. Hamzi, and H. Abbad. 2022. "Effect of Porosity on the Thermal Buckling of Functionally Graded Material (FGM) Sandwich Plates under Different Boundary Conditions." *Mechanics Based Design of Structures and Machines* 1–23. https://doi.org/10.1080/15397734.2022.2148691

Civalek, Ö., B. Uzun, and M. Ö. Yaylı. 2022. "An Effective Analytical Method for Buckling Solutions of a Restrained FGM Nonlocal Beam." *Computational and Applied Mathematics* 41 (2): 1–20. https://doi.org/10.1007/s40314-022-01761-1

Derikvand, M., F. Farhatnia, and D. H. Hodges. 2021. "Functionally Graded Thick Sandwich Beams with Porous Core: Buckling Analysis via Differential Transform Method." *Mechanics Based Design of Structures and Machines* 51 (7): 3650–3677. https://doi.org/10.1080/15397734.2021.1931309

Ebrahimi, F., A. Seyfi, M. Nouraei, and P. Haghi. 2022. "Influence of Magnetic Field on the Wave Propagation Response of Functionally Graded (FG) Beam Lying on Elastic Foundation in Thermal Environment." *Waves in Random and Complex Media* 32 (5): 2158–2176. https://doi.org/10.1080/17455030.2020.1847359

Ebrahimi, F., and A. Jafari. 2016. "A Higher-Order Thermomechanical Vibration Analysis of Temperature-Dependent FGM Beams with Porosities." *Journal of Engineering* 2016: 1–20. https://doi.org/10.1155/2016/9561504

Ebrahimi, F., and E. Salari. 2015a. "Thermo-Mechanical Vibration Analysis of Nonlocal Temperature-Dependent FG Nanobeams with Various Boundary Conditions." *Composites Part B: Engineering* 78: 272–290. https://doi.org/10.1016/j.compositesb.2015.03.068

Ebrahimi, F., and E. Salari. 2015b. "Thermal Buckling and Free Vibration Analysis of Size Dependent Timoshenko FG Nanobeams in Thermal Environments." *Composite Structures* 128: 363–380. https://doi.org/10.1016/j.compstruct.2015.03.023

Ebrahimi, F., and M. Sepahvand. 2023. "Wave Propagation Analysis of Cylindrical Sandwich Shell with Auxetic Core Utilizing First-Order Shear Deformable Theory (FSDT)." *Mechanics Based Design of Structures and Machines* 1–25. https://doi.org/10.1080/15397734.2022.2159835

Ellali, M., M. Bouazza, and K. Amara. 2022. "Thermal Buckling of a Sandwich Beam Attached with Piezoelectric Layers via the Shear Deformation Theory." *Archive of Applied Mechanics* 92 (3): 657–665. https://doi.org/10.1007/s00419-021-02094-x

Eltaher, M. A., A. M. Kabeel, K. H. Almitani, and A. M. Abdraboh. 2018. "Static Bending and Buckling of Perforated Nonlocal Size-Dependent Nanobeams." *Microsystem Technologies* 24 (12): 4881–4893. https://doi.org/10.1007/s00542-018-3905-3

Emeje, M. O., I. C. Obidike, E. I. Akpabio, and S. I. Ofoefule. 2012. *Nanotechnology in Drug Delivery*, 57–67. Rijeka: Intech.

Eringen, A. C. 1983. "On Differential Equations of Nonlocal Elasticity and Solutions of Screw Dislocation and Surface Waves." *Journal of Applied Physics* 54 (9): 4703–4710. https://doi.org/10.1063/1.332803

Esen, I. 2019. "Dynamic Response of a Functionally Graded Timoshenko Beam on Two-Parameter Elastic Foundations Due to a Variable Velocity Moving Mass." *International Journal of Mechanical Sciences* 153–154: 21–35. https://doi.org/10.1016/j.ijmecsci.2019.01.033

Eyvazian, A., C. Zhang, Ö. Civalek, A. Khan, T. A. Sebaey, and N. Farouk. 2022. "Wave Propagation Analysis of Sandwich FGM Nanoplate Surrounded by Viscoelastic Foundation." *Archives of Civil and Mechanical Engineering* 22 (4): 1–10. https://doi.org/10.1007/s43452-022-00474-w

Feizi, S., S. Javadiyan, C. M. Cooksley, G. Shaghayegh, A. J. Psaltis, P. J. Wormald, and S. Vreugde. 2021. "Green Synthesized Colloidal Silver is Devoid of Toxic Effects on Primary Human Nasal Epithelial Cells *In Vitro*." *Food and Chemical Toxicology* 157: 112606. https://doi.org/10.1016/j.fct.2021.112606

Feri, M., M. Krommer, and A. Alibeigloo. 2021. "Three-Dimensional Static Analysis of a Viscoelastic Rectangular Functionally Graded Material Plate Embedded between Piezoelectric Sensor and Actuator Layers." *Mechanics Based Design of Structures and Machines* 51 (7): 3843–3867. https://doi.org/10.1080/15397734.2021.1943673

Garg, A., H. D. Chalak, and A. Chakrabarti. 2020. "Comparative Study on the Bending of Sandwich FGM Beams Made up of Different Material Variation Laws Using Refined Layerwise Theory." *Mechanics of Materials* 151: 103634. https://doi.org/10.1016/j.mechmat.2020.103634

Ghayesh, M. H., A. Farajpour, and H. Farokhi. 2020. "Effect of Flow Pulsations on Chaos in Nanotubes Using Nonlocal Strain Gradient Theory." *Communications in Nonlinear Science and Numerical Simulation* 83: 105090. https://doi.org/10.1016/j.cnsns.2019.105090

Gul, U., and M. Aydogdu. 2021. "Buckling Analysis of Functionally Graded Beams with Periodic Nanostructures Using Doublet Mechanics Theory." *Journal of the Brazilian Society of Mechanical Sciences and Engineering* 43 (5): 1–8. https://doi.org/10.1007/s40430-021-02972-z

Hamza Madjid, B., and B. Bouderba. 2022. "Buckling Analysis of FGM Plate Exposed to Different Loads Conditions." *Mechanics Based Design of Structures and Machines* 51 (12): 6798–6813. https://doi.org/10.1080/15397734.2022.2068576

Hassaine, N., N. Touat, M. Dahak, A. Fellah, and A. Saimi. 2022. "Study of Crack's Effect on the Natural Frequencies of bi-Directional Functionally Graded Beam." *Mechanics Based Design of Structures and Machines* 52 (1):375–385. https://doi.org/10.1080/15397734.2022.2113408

Hung, P. T., C. H. Thai, and P. Phung-Van. 2023a. "Isogeometric Bending and Free Vibration Analyses of Carbon Nanotube-Reinforced Magneto-Electric-Elastic Microplates Using a Four Variable Refined Plate Theory." *Computers and Structures* 287: 107121. https://doi.org/10.1016/j.compstruc.2023.107121

Hung, P. T., C. H. Thai, and P. Phung-Van. 2023b. "A C0-HSDT Free Vibration of Magneto-Electro-Elastic Functionally Graded Porous Plates Using a Moving Kriging Meshfree Method." *Aerospace Science and Technology* 137: 108266. https://doi.org/10.1016/j.ast.2023.108266

Karakoti, A., S. Pandey, and V. R. Kar. 2022. "Nonlinear Transient Analysis of Porous P-FGM and S-FGM Sandwich Plates and Shell Panels under Blast Loading and Thermal Environment." *Thin-Walled Structures* 173: 108985. https://doi.org/10.1016/j.tws.2022.108985

Karami, B., and M. H. Ghayesh. 2023. "Vibration Characteristics of Sandwich Microshells with Porous Functionally Graded Face Sheets." *International Journal of Engineering Science* 189: 103884. https://doi.org/10.1016/j.ijengsci.2023.103884

Karami, B., D. Shahsavari, and L. Li. 2018. "Temperature-Dependent Flexural Wave Propagation in Nanoplate-Type Porous Heterogenous Material Subjected to in-Plane Magnetic Field." *Journal of Thermal Stresses* 41 (4): 483–499. https://doi.org/10.1080/01495739.2017.1393781

Karami, B., M. Janghorban, and A. Tounsi. 2017. "Effects of Triaxial Magnetic Field on the Anisotropic Nanoplates." *Steel and Composite Structures* 25: 361–374. https://doi.org/10.12989/scs.2017.25.3.361

Karami, B., M. Janghorban, and A. Tounsi. 2018. "Variational Approach for Wave Dispersion in Anisotropic Doubly-Curved Nanoshells Based on a New Nonlocal Strain Gradient Higher Order Shell Theory." *Thin-Walled Structures* 129: 251–264. https://doi.org/10.1016/j.tws.2018.02.025

Karami, B., M. Janghorban, and A. Tounsi. 2019. "On Pre-Stressed Functionally Graded Anisotropic Nanoshell in Magnetic Field." *Journal of the Brazilian Society of Mechanical Sciences and Engineering* 41 (11): 1–17. https://doi.org/10.1007/s40430-019-1996-0

Karami, B., M. Janghorban, and A. Tounsi. 2020. "Novel Study on Functionally Graded Anisotropic Doubly Curved Nanoshells." *The European Physical Journal Plus* 135 (1): 31. https://doi.org/10.1140/epjp/s13360-019-00079-y

Karami, B., M. Janghorban, and H. Fahham. 2022. "Forced Vibration Analysis of Anisotropic Curved Panels via a Quasi-3D Model in Orthogonal Curvilinear Coordinate." *Thin-Walled Structures* 175: 109254. https://doi.org/10.1016/j.tws.2022.109254

Karami, B., M. Janghorban, and L. Li. 2018. "On Guided Wave Propagation in Fully Clamped Porous Functionally Graded Nanoplates." *Acta Astronautica* 143: 380–390. https://doi.org/10.1016/j.actaastro.2017.12.011

Katili, I., J. L. Batoz, S. Bouabdallah, I. J. Maknun, and A. M. Katili. 2023. "Discrete Shear Projection Method for Mechanical Buckling Analysis of FGM Sandwich Plates." *Composite Structures* 312: 116825. https://doi.org/10.1016/j.compstruct.2023.116825

Khalili, S. M. R., A. A. Jafari, and S. A. Eftekhari. 2010. "A Mixed Ritz-DQ Method for Forced Vibration of Functionally Graded Beams Carrying Moving Loads." *Composite Structures* 92 (10): 2497–2511. https://doi.org/10.1016/j.compstruct.2010.02.012

Kiani, Y., and M. R. R. Eslami. 2013. "An Exact Solution for Thermal Buckling of Annular FGM Plates on an Elastic Medium." *Composites Part B: Engineering* 45 (1): 101–110. https://doi.org/10.1016/j.compositesb.2012.09.034

Kim, H. J., and J. R. Cho. 2023. "A Numerical Study on Free Vibration Analysis of Detailed and Homogenized Models for FG-CNTRC Beams." *Journal of Mechanical Science and Technology* 37 (1): 229–238. https://doi.org/10.1007/s12206-022-1224-1

Kraus, J. 1992. *Electromagnetics*. New York: McGraw-Hill.

Kumar Sah, S., and A. Ghosh. 2022. "Influence of Porosity Distribution on Free Vibration and Buckling Analysis of Multi-Directional Functionally Graded Sandwich Plates." *Composite Structures* 279: 114795. https://doi.org/10.1016/j.compstruct.2021.114795

Lal, A., and K. Markad. 2021. "Static and Dynamic Nonlinear Stability Analyses of Hybrid Sandwich Composite Beams under Variable in-Plane Loads." *Journal of Mechanical Science and Technology* 35 (9): 3895–3908. https://doi.org/10.1007/s12206-021-0803-x

Le, C. I., N. A. T. Le, and D. K. Nguyen. 2021. "Free Vibration and Buckling of Bidirectional Functionally Graded Sandwich Beams Using an Enriched Third-Order Shear Deformation Beam Element." *Composite Structures* 261: 113309. https://doi.org/10.1016/j.compstruct.2020.113309

Li, L., and Y. Hu. 2016. "Nonlinear Bending and Free Vibration Analyses of Nonlocal Strain Gradient Beams Made of Functionally Graded Material." *International Journal of Engineering Science* 107: 77–97. https://doi.org/10.1016/j.ijengsci.2016.07.011

Li, Z., J. Liu, B. Hu, Y. Wang, and H. Shen. 2023. "Wave Propagation Analysis of Porous Functionally Graded Piezoelectric Nanoplates with a Visco-Pasternak Foundation." *Applied Mathematics and Mechanics* 44 (1): 35–52. https://doi.org/10.1007/s10483-023-2953-7

Lim, C. W., G. Zhang, and J. N. Reddy. 2015. "A Higher-Order Nonlocal Elasticity and Strain Gradient Theory and Its Applications in Wave Propagation." *Journal of the Mechanics and Physics of Solids* 78: 298–313. https://doi.org/10.1016/j.jmps.2015.02.001

Liu, J., B. He, W. Ye, and F. Yang. 2021. "High Performance Model for Buckling of Functionally Graded Sandwich Beams Using a New Semi-Analytical Method." *Composite Structures* 262: 113614. https://doi.org/10.1016/j.compstruct.2021.113614

Liu, J., C. Hao, W. Ye, and Q. Zang. 2023. "Application of a New Semi-Analytic Method in Bending Behavior of Functionally Graded Material Sandwich Beams." *Mechanics Based Design of Structures and Machines* 51 (4): 2130–2153. https://doi.org/10.1080/15397734.2021.1890615

Liu, J., C. Hao, Y. Zhou, and W. Ye. 2021. "Dynamic Analysis of Functionally Graded Sandwich Beams Using a Semi-Analytic Method Named Scaled Boundary Finite Element Method." *Engineering Analysis with Boundary Elements* 130: 161–175. https://doi.org/10.1016/j.enganabound.2021.05.010

Ma, H. M., X.-L. Gao, and J. N. Reddy. 2008. "A Microstructure-Dependent Timoshenko Beam Model Based on a Modified Couple Stress Theory." *Journal of the Mechanics and Physics of Solids* 56 (12): 3379–3391. https://doi.org/10.1016/j.jmps.2008.09.007

Mirzavand Borojeni, B., S. Shams, M. R. Kazemi, and M. Rokn-Abadi. 2022. "Effect of Temperature and Magnetoelastic Loads on the Free Vibration of a Sandwich Beam with Magnetorheological Core and Functionally Graded Material Constraining Layer." *Acta Mechanica* 233 (11): 4939–4959. https://doi.org/10.1007/s00707-022-03316-1

Morigi, V., A. Tocchio, C. Bellavite Pellegrini, J. H. Sakamoto, M. Arnone, and E. Tasciotti. 2012. "Nanotechnology in Medicine: From Inception to Market Domination." *Journal of Drug Delivery* 2012: 389485–389487. https://doi.org/10.1155/2012/389485

Nguyen, D. K., B. S. Gan, and T. H. Le. 2013. "Dynamic Response of Non-Uniform Functionally Graded Beams Subjected to a Variable Speed Moving Load." *Journal of Computational Science and Technology* 7 (1): 12–27. https://doi.org/10.1299/jcst.7.12

Nguyen, D. K., T. T. H. Bui, T. T. H. Tran, and S. Alexandrov. 2022. "Large Deflections of Functionally Graded Sandwich Beams with Influence of Homogenization Schemes." *Archive of Applied Mechanics* 92 (6): 1757–1775. https://doi.org/10.1007/s00419-022-02140-2

Nguyen, L. B., H. Nguyen-Xuan, C. H. Thai, and P. Phung-Van. 2023. "A Size-Dependent Effect of Smart Functionally Graded Piezoelectric Porous Nanoscale Plates." *International Journal of Mechanics and Materials in Design* 19 (4): 817–830. https://doi.org/10.1007/s10999-023-09660-x

Nguyen, V. D., and V. B. Phung. 2023. "Static Bending, Free Vibration, and Buckling Analyses of Two-Layer FGM Plates with Shear Connectors Resting on Elastic Foundations." *Alexandria Engineering Journal* 62: 369–390. https://doi.org/10.1016/j.aej.2022.07.038

Nguyen, V. L., M. T. Tran, S. Limkatanyu, and J. Rungamornrat. 2022. "Free Vibration Analysis of Rotating FGP Sandwich Cylindrical Shells with Metal-Foam Core Layer." *Mechanics of Advanced Materials and Structures* 30 (16): 3318–3331. https://doi.org/10.1080/15376494.2022.2073410

Phung-Van, P., A. J. M. Ferreira, H. Nguyen-Xuan, and C. H. Thai. 2021. "Scale-Dependent Nonlocal Strain Gradient Isogeometric Analysis of Metal Foam Nanoscale Plates with Various Porosity Distributions." *Composite Structures* 268: 113949. https://doi.org/10.1016/j.compstruct.2021.113949

Phung-Van, P., and C. H. Thai. 2022. "A Novel Size-Dependent Nonlocal Strain Gradient Isogeometric Model for Functionally Graded Carbon Nanotube-Reinforced Composite Nanoplates." *Engineering with Computers* 38 (S3): 2027–2040. https://doi.org/10.1007/s00366-021-01353-3

Phung-Van, P., Q. X. Lieu, A. J. M. Ferreira, and C. H. Thai. 2021. "A Refined Nonlocal Isogeometric Model for Multilayer Functionally Graded Graphene Platelet-Reinforced Composite Nanoplates." *Thin-Walled Structures* 164: 107862. https://doi.org/10.1016/j.tws.2021.107862

Rahmani, O., and O. Pedram. 2014. "Analysis and Modeling the Size Effect on Vibration of Functionally Graded Nanobeams Based on Nonlocal Timoshenko Beam Theory." *International Journal of Engineering Science* 77: 55–70. https://doi.org/10.1016/j.ijengsci.2013.12.003

Reddy, J. N. 2007. "Nonlocal Theories for Bending, Buckling and Vibration of Beams." *International Journal of Engineering Science* 45 (2–8): 288–307. https://doi.org/10.1016/j.ijengsci.2007.04.004

Sahoo, Brundaban, N. Sharma, Bamadev Sahoo, P. Malhari Ramteke, S. Kumar Panda, and S. R. Mahmoud. 2022. "Nonlinear Vibration Analysis of FGM Sandwich Structure under Thermal Loadings." *Structures* 44: 1392–1402. https://doi.org/10.1016/j.istruc.2022.08.081

Sayyad, A. S., Y. M. Ghugal, and T. Kant. 2023. "Higher-Order Static and Free Vibration Analysis of Doubly-Curved FGM Sandwich Shallow Shells." *Forces in Mechanics* 11: 100194. https://doi.org/10.1016/j.finmec.2023.100194

Shahsavari, D., and B. Karami. 2022. "Assessment of Reuss, Tamura, and LRVE Models for Vibration Analysis of Functionally Graded Nanoplates." *Archives of Civil and Mechanical Engineering* 22 (2): 1–13. https://doi.org/10.1007/s43452-022-00409-5

Shahsavari, D., B. Karami, and A. Tounsi. 2023. "Wave Propagation in a Porous Functionally Graded Curved Viscoelastic Nano-Size Beam." *Waves in Random and Complex Media* 1–22. https://doi.org/10.1080/17455030.2022.2164376

Şimşek, M., and T. Kocatürk. 2009. "Free and Forced Vibration of a Functionally Graded Beam Subjected to a Concentrated Moving Harmonic Load." *Composite Structures* 90 (4): 465–473. https://doi.org/10.1016/j.compstruct.2009.04.024

Sina, S. A., H. M. Navazi, and H. Haddadpour. 2009. "An Analytical Method for Free Vibration Analysis of Functionally Graded Beams." *Materials and Design* 30 (3): 741–747. https://doi.org/10.1016/j.matdes.2008.05.015

Singh, T., S. Shukla, P. Kumar, V. Wahla, and V. K. Bajpai. 2017. "Application of Nanotechnology in Food Science: Perception and Overview." *Frontiers in Microbiology* 8: 1501. https://doi.org/10.3389/fmicb.2017.01501

Thai, C. H., A. M. J. Fereira, H. Nguyen-Xuan, P. T. Hung, and P. Phung-Van. 2023. "A Nonlocal Strain Gradient Isogeometric Model for Free Vibration Analysis of Magneto-Electro-Elastic Functionally Graded Nanoplates." *Composite Structures* 316: 117005. https://doi.org/10.1016/j.compstruct.2023.117005

Thai, C. H., P. T. Hung, H. Nguyen-Xuan, and P. Phung-Van. 2023. "A Size-Dependent Meshfree Approach for Magneto-Electro-Elastic Functionally Graded Nanoplates Based on Nonlocal Strain Gradient Theory." *Engineering Structures* 292: 116521. https://doi.org/10.1016/j.engstruct.2023.116521

Thrall, J. H. 2004. "Nanotechnology and Medicine." *Radiology* 230 (2): 315–318. https://doi.org/10.1148/radiol.2302031698

Touloukian, Y. S. 1966. *Thermophysical Properties of High Temperature Solid Materials. Volume 4. Oxides and Their Solutions and Mixtures*. Part 1, Vol. 1. New York, NY: Macmillan.

Touloukian, Y. S. 1967. *Thermophysical Properties of High Temperature Solid Materials*. New York, NY: Macmillan.

Tounsi, A., Houari, M. S. A., Benyoucef, S, and Adda Bedia, E. A. 2013. "A Refined Trigonometric Shear Deformation Theory for Thermoelastic Bending of Functionally Graded Sandwich Plates." *Aerospace Science and Technology* 24 (1): 209–220. https://doi.org/10.1016/j.ast.2011.11.009

Varadan, V. K., A. S. Pillai, D. Mukherji, M. Dwivedi, and L. Chen. 2010. *Nanoscience and Nanotechnology in Engineering*. Singapore: World Scientific. https://doi.org/10.1142/7364

Vattré, A., and E. Pan. 2021. "Thermoelasticity of Multilayered Plates with Imperfect Interfaces." *International Journal of Engineering Science* 158: 103409. https://doi.org/10.1016/j.ijengsci.2020.103409

Vattré, A., and E. Pan. 2022. "Dislocation Singularities in Layered Magneto-Electro-Elastic Plates." *International Journal of Engineering Science* 181: 103765. https://doi.org/10.1016/j.ijengsci.2022.103765

Vu, A. N. T., N. A. T. Le, and D. K. Nguyen. 2021. "Dynamic Behaviour of Bidirectional Functionally Graded Sandwich Beams under a Moving Mass with Partial Foundation Supporting Effect." *Acta Mechanica* 232 (7): 2853–2875. https://doi.org/10.1007/s00707-021-02948-z

Xiao, J., and J. Wang. 2023. "Nonlinear Vibration of FGM Sandwich Nanoplates with Surface Effects." *Acta Mechanica Solida Sinica* 36 (2): 274–281. https://doi.org/10.1007/s10338-022-00371-y

Xu, X., B. Karami, and D. Shahsavari. 2021. "Time-Dependent Behavior of Porous Curved Nanobeam." *International Journal of Engineering Science* 160: 103455. https://doi.org/10.1016/j.ijengsci.2021.103455

Yas, M. H., and S. Mohammadi. 2020. "Experimental and Theoretical Studies of Free Vibration of a Sandwich Functionally Graded Nanocomposite Beam under Thermal Condition." *SN Applied Sciences* 2 (7): 1–16. https://doi.org/10.1007/s42452-020-3080-x

Ye, W., J. Liu, Q. Zang, Z. Yin, and G. Lin. 2022. "Buckling Analysis of Three-Dimensional Functionally Graded Sandwich Plates Using Two-Dimensional Scaled Boundary Finite Element Method." *Mechanics of Advanced Materials and Structures* 29 (17): 2468–2483. https://doi.org/10.1080/15376494.2020.1866125

Youzera, H., M. Mohamed, S. Saleh, M. H. Ghazwani, S. A. Meftah, A. Tounsi, and T. Cuong-Le. 2023. "Nonlinear Damping and Forced Vibration Analysis of Sandwich Functionally Graded Material Beams with Composite Viscoelastic Core Layer." *Mechanics Based Design of Structures and Machines* 1–20. https://doi.org/10.1080/15397734.2023.2229911

Zhang, D. G. 2014. "Thermal Post-Buckling and Nonlinear Vibration Analysis of FGM Beams Based on Physical Neutral Surface and High Order Shear Deformation Theory." *Meccanica* 49 (2): 283–293. https://doi.org/10.1007/s11012-013-9793-9

Zhang, W., C. Wang, Y. Wang, J. J. Mao, and Y. Liu. 2022. "Nonlinear Vibration Responses of Lattice Sandwich Beams with FGM Facesheets Based on an Improved Thermo-Mechanical Equivalent Model." *Structures* 44: 920–932. https://doi.org/10.1016/j.istruc.2022.08.052

Appendix A

The coefficients of symmetric M_{ij} and K_{ij} matrices are described as follows:

$$
\begin{aligned}
& M_{11} = -I_0 c_1, \ \ M_{12} = -I_1 \beta c_1, \ \ M_{13} = I_3 c_1, \ \ M_{21} = M_{12}, \\
& M_{22} = \left(I_0 + I_2 \beta^2\right) c_1, \ \ M_{23} = -I_4 \beta c_1, \ \ M_{31} = M_{13}, \\
& M_{32} = M_{23}, \ \ M_{33} = I_5 c_1, \ \ K_{11} = -A_{11} c_2 \beta^2, \ \ K_{12} = B_{11} c_2 \beta^3, \\
& K_{13} = -C_{11} c_2 \beta^2, \ \ K_{21} = B_{11} \beta^3 c_2, \\
& K_{22} = -D_{11} \beta^4 c_2 + \left(-N^T \beta^2 + \varepsilon h \bar{H}_x^2 \beta^2 + k_p \beta^2 + k_w\right) c_1, \ \ K_{23} = -F_{11} \beta^3 c_2, \\
& K_{31} = K_{13}, \ \ K_{32} = K_{23}, \ \ K_{33} = \left(H_{11} \beta^2 + J_{66}\right) c_2, \\
& c_1 = 1 + (e_0 a)^2 \beta^2, \ \ c_2 = 1 + l_m^2 \beta^2
\end{aligned}
\tag{A1}
$$